Travelling Wave Based DC Line Fault Location in VSC HVDC Systems

By

Amila Nuwan Pathirana

A Thesis submitted to the Faculty of Graduate Studies of

The University of Manitoba

in partial fulfilment of the requirements of the degree of

MASTER OF SCIENCE

Department of Electrical and Computer Engineering

University of Manitoba

Winnipeg

Abstract

Travelling wave based fault location techniques work well for line commutated converter (LCC) based high voltage direct current (HVDC) transmission lines, but the large capacitors at the DC line terminals makes application of the same techniques for voltage source converter (VSC) based HVDC schemes challenging. A range of possible signals for detecting the fault generated travelling wave arrival times was investigated. Considering a typical VSC HVDC system topology and based on the study, an efficient detection scheme was proposed. In this scheme, the rate of change of the current through the surge capacitor located at each line terminal is measured by using a Rogowski coil and compared with a threshold to detect the wave fronts. Simulation studies in PSCAD showed that fault location accuracy of ±100 m is achievable for a 300 km long cable and 1000 km long overhead line. Experimental measurements in a practical HVDC converter station confirmed the viability of the proposed measurement scheme.

Acknowledgments

I would like to thank my advisor, prof. Athula Rajapakse, for his excellent guidance and advice throughout the course of this work. The financial support received from Manitoba HVDC research centre and NSERC is greatly appreciated.

Special thanks go to Mr. Ervin Dirks who supported me during experiments in the machines lab of University of Manitoba and Mr. Jean Sebastien Stoezel of HVDC Research Center who helped during the testing of Rogowski coil. Comments made by Mr. Randy Wachal Manitoba of HVDC Research Centre are greatly appreciated.

I would like to extend my special thanks to Mr. Kasun Nanayakkara for the comments and help received during the research period. Furthermore I would like to thank the staff and all of my friends in department of Electrical and Computer Engineering for their continuous encouragement and making the time I spend at the University of Manitoba a pleasant experience.

Finally, I would like to extend my heartiest gratitude to my wife and my parents. They always understood and encouraged me during my hard times.

Amila Nuwan Pathirana

December 2012

Dedication

To my loving parents

Table of Contents

Abstract ii
Acknowledgments iii
Dedication iv
Table of Contents v
List of Figures viii
List of Tables xii
List of Abbreviations xiii

Introduction **1**

1.1 Background 1
1.2 Problem definition 2
1.3 Motivation behind the research 3
1.4 Objective of the research 4
1.5 Thesis overview 5

Literature Survey **7**

2.1 Introduction 7
2.2 Types of faults 7
2.3 Expected characteristics of fault locators 8
2.4 Line fault location methods 8
2.4.1 Techniques based on impedance measurement 9

2.4.2 Fault location using frequency spectrums 10
2.4.3 Machine learning based fault location approaches 11
2.4.4 Travelling wave based fault location 12
2.5 Current LFL technology 19

Surge Detection Method 22

3.1 Introduction 22
3.2 Sensors for measuring transient signals 23
3.2.1 Coaxial shunts 23
3.2.2 Current transformers 23
3.2.3 Hall effect sensors 24
3.2.4 Rogowski coils 24
3.2.5 Voltage dividers 25
3.3 Signals available for travelling wave detection 25
3.4 Analysis of wave front detection 28
3.5 Experimental results 38
3.6 Concluding remarks 40

Modelling of Rogowski Coil 42

4.1 Introduction 42
4.2 Rogowski coil models 43
4.3 Verification of the Rogowski coil model 47
4.4 Concluding remarks 50

Line Fault Location Performance 51

5.1 Introduction 51
5.2 Simulated system 51
5.3 Fault location calculation 55
5.4 Threshold setting 56

5.5 Modal transform 66
5.5.1 Modal transformation of the Rogowski coil voltages 67
5.6 Fault location with filtered signals 70
5.7 VSC HVDC scheme with overhead lines 80
5.8 Fault location accuracies 81
5.9 Concluding remarks 85

Conclusions and Future Work **87**

6.1 Conclusions 87
6.2 Future work 89
Bibliography 90

List of Figures

Figure 2-1 Voltage profile of Inductive termination 10

Figure 2-2 Schematic of a single-phase lossless line (top) and equivalent circuit representing an elemental length *dx* of the line (bottom) 14

Figure 2-3 Reflection of travelling wave at a junction 16

Figure 2-4 Lattice diagram to illustrate the travelling wave flow along the transmission line 18

Figure 3-1 Voltage travelling wave $v(xo,t)$ arriving at a capacitively terminated end of a line and the voltage observed at the terminal $vo(xo,t)$ 27

Figure 3-2 Test system used for the simulations 30

Figure 3-3 Parameters of the cable 30

Figure 3-4 Proposed termination 31

Figure 3-5(a) Cable terminal voltage variation for a solid P-G fault 70 km away from Converter-1 (b) Zoomed view 32

Figure 3-6 Terminal voltage waveforms with and without a series inductor for a solid P-G fault 70 km away from Converter-1. 33

Figure 3-7 Terminal current variation with and without a series inductor (1 mH) for a solid P-G fault 70 km away from Converter-1 34

Figure 3-8 Surge capacitor current variation with and without a series inductor (1 mH) for a solid P-G fault 70 km away from Converter-1 35

Figure 3-9 Surge capacitor current variation with and without a series inductor (10 mH) for a solid P-G fault 70 km away from Converter-1 35

Figure 3-10 Variation of the rate of change of the surge capacitor current for a solid P-G fault 70 km away from Converter-1 (surge capacitance fixed at 100 nF)....36

Figure 3-11 Variation of the rate of change of the surge capacitor current for a solid P-G fault 70 km away from Converter-1(series inductance fixed at 1 mH) 37

Figure 3-12 Termination of the overhead line at Dorsey converter station 39

Figure 3-13(a) Rogowski coil voltage for a fault 356 km away from Dorsey converter station (b) Zoomed view indicating the noise level....40

Figure 4-1 (a) Rogowski coil, (b) Expanded view of a small section showing details and (c) Equivalent circuit....44

Figure 4-2 Rogowski coil test setup....48

Figure 4-3 Injected primary current to the Rogowski coil 49

Figure 4-4 Simulated and actual Rogowski coil output voltages....49

Figure 4-5 Primary current injected to the Rogowski coil....50

Figure 4-6 Simulated and actual Rogowski coil output voltages....50

Figure 5-1 400 kV VSC HVDC system 52

Figure 5-2 Parameters of the Cable 52

Figure 5-3 Variations of the terminal voltages (a) Positive poles (b) Negative poles, the terminal currents (c) Positive poles (d) Negative poles, the surge capacitor currents (e) Positive pole (f) Negative pole and the Rogowski coil voltages (g) Positive pole (h) Negative pole for solid pole-to-ground fault on positive pole 130 km from Converter-1....54

Figure 5-4 Threshold selection criteria....57

Figure 5-5 Threshold settings....58

Figure 5-6 Converter 1 side Rogowski coil voltage for a solid fault 130 km from Converter-1. 59

Figure 5-7 Converter-2 side Rogowski coil voltage for a solid fault 130 km from Converter-1. 59

Figure 5-8 Variation of the fault location error with the threshold level for a fault 30km the Converter -1....62

Figure 5-9 Variation of the fault location error with the threshold level for a fault 50km the Converter -1 62

Figure 5-10 Variation of the fault location error with the threshold level for a fault 130km the Converter -1 63

Figure 5-11 Variation of the fault location error with the threshold level for a fault 160km the Converter -1 63

Figure 5-12 Variation of the fault location error with the threshold level for a fault 220 km the Converter -1 64

Figure 5-13 Variations of the fault location error with the threshold for a fault 50km from the Converter -1 (for low threshold values) 65

Figure 5-14Terminal voltages 71

Figure 5-15Frequency spectrum of terminal voltages 71

Figure 5-16 Characteristics of the 5th order low pass Butterworth filter with a cut-off frequency of 100 kHz (a) Magnitude (b) Phase 73

Figure 5-17Filtered terminal voltages 74

Figure 5-18Frequency spectrum filtered terminal voltages 74

Figure 5-19 (a) filtered and unfiltered Rogowski coil voltages for a solid P-G fault 130 km away from the Converter-1. (b) Zoomed y-axis during steady state. 75

Figure 5-20 Variation of fault location error for solid faults when the detection signal is filtered with a 100 kHz low pass filter 79

Figure 5-21 Variation of fault location error for high resistance faults (100Ω) when the detection signal is filtered with a 100 kHz low pass filter 79

Figure 5-22Configurationof the transmission line 81

Figure 5-23 Variation of the fault location error with threshold for a fault 600 km away from the Converter-1. 82

Figure 5-24 Variation of the fault location error with threshold for a fault 300 km away from the Converter-1. 83

Figure 5-25 Variation of the fault location error with threshold for a fault 100 km away from the Converter-1 83

Figure 5-26 Fault location errors for solid faults along 1000 km overhead line. 84

Figure 5-27 Fault location errors for faults with fault resistance of 100Ω along 1000 km overhead line 84

List of Tables

Table 3-1 Parameters of the Rogowski coil used for the experiment in Dorsey converter station.....39

Table 4-1 Parameters of the Rogowski coil Prototype 47

Table 5-1 – Rogowski coil parameters.....53

Table 5-2 Comparison of fault location errors for different threshold settings and for visual inspection method.....61

Table 5-3 Fault location error comparison with modal transform for solid faults.....69

Table 5-4 Fault location error comparison with modal transform for faults with 100Ω fault resistance.....69

Table 5-5 Fault location errors with filtered detection signals (Threshold-1 / Solid fault).....76

Table 5-6Fault location errors with filtered detection signals (Threshold-1/ Fault resistance 100Ω)..77

Table 5-7 Fault location errors with filtered detection signals(Threshold-10 / Solid fault).....77

Table 5-8 Fault location errors with filtered detection signals (Threshold 10 / Fault resistance 100Ω). 78

List of Abbreviations

AC	Alternating current
A/D	Analog to Digital
CT	Current Transformer
DAQ	Data acquisition
DC	Direct current
DFT	Discrete Fourier transform
EMT	Electromagnetic transient
emf	Electro motive force
GPS	Global positioning system
HVDC	High voltage direct current
IBGT	Insulated gate bipolar transistor
LCC	Line commutated converter
LFL	Line fault locator
P-G	Pole to Ground
PSCAD/EMTDC	Electromagnetic power transient software
ROW	Right of way
VSC	Voltage source converter

Chapter 1

Introduction

1.1 Background

With the increasing demand for electricity, new generation has to be developed. Many new generation sources, specially the renewable sources such as large onshore and offshore wind farms are located far from the load centres. Therefore, long transmission lines and cables with large transmission capacity are needed to interconnect the generation and the load centres. High Voltage Direct Current (HVDC) transmission has distinct advantages when transmitting large amounts of power over long distances. Controllability of HVDC systems provides further operational benefits to the power systems. Therefore, use of HVDC transmission in power systems is increasing continuously. Conventional HVDC schemes use thyristor based line commutated converters (LCCs). However, new IGBT based voltage source converter (VSC) HVDC systems are gradually gaining ground as the technology has significantly improved in the last few years.

Transmission lines and cables are affected by faults, lightning strikes, and equipment failures. Outage of a HVDC transmission line or cable can result in supply interruptions, loss of revenue, and operational problems such as reduced stability margins. Thus the HVDC transmission lines and cables used to transfer bulk power need to be repaired as quickly as possible. Repair times can be significantly reduced if the locations of permanent faults can be determined accurately and quickly. Fault location is a major time consuming factor when foot patrols are relied upon in long lines built over rough terrain. There are several methods for fault location in transmission lines and cables [1]. However, travelling wave based fault location is the most common method applied in HVDC transmission lines. In this approach, the location of a fault is determined based on the time taken by the fault generated travelling waves to propagate to the overhead line or cable terminal points. Fault location using travelling waves has become more accurate with advancement of the technology. Modern data acquisition (DAQ) systems are capable of synchronizing with the highly accurate time signal received from global positioning system (GPS) and collecting time tagged data samples at high sampling rates [2].

1.2 Problem definition

Application of travelling wave based fault location techniques in AC transmission systems and LCC HVDC systems have been studied extensively [2]-[10]. Arrival of a travelling wave is manifested as a transient change in the voltage (and/or current) at the respective terminal. Sharpness of the wave fronts is critical for accurate detection of the travelling wave arrival times, which are the main inputs for travelling based fault location calculation. Imprecise detection of travelling wave arrival times can increase the errors in fault location. The shape of the fault

generated voltage and current waves measured at a converter terminal can vary depending on the type of HVDC converter used [11]-[12]. The large smoothing inductor (in the range of 0.5 H) employed between the converter and the line/cable terminals in LCC HVDC systems essentially isolate high frequency voltage/current signals arriving along the line in to the converter. Therefore, sharp voltage transients can be observed at the line or cable terminals. In VSC HVDC schemes, such sharp voltage transients may not be observed due to the presence of large DC capacitor [13] and the absence of large smoothing inductor.

It is expected that VSC HVDC schemes with long cables (>250 km) will be developed for connecting offshore wind farms and in DC grids. A literature survey did not yield any publications dealing with the fault location in VSC HVDC schemes with such long cable connections. In long cables, the magnitude of travelling waves can decrease to a level that makes accurate determination of the travelling wave arrival time difficult due to attenuation of the travelling wave during the propagation. The large DC capacitance at the converter terminal makes the situation further difficult. The other main challenge in travelling wave based fault location is the limited measurement bandwidth of the transducers used to detect the fault generated current or voltage waveforms.

1.3 Motivation behind the research

Quick repairing is essential for minimizing the down time and outage costs, especially in the case of HVDC transmission systems that are employed to carry large amounts of power or provide stability to the power system. Accurate fault locator ensures rapid dispatching of repair crews to the fault location which is important for deciding the cause of the fault and required repair work.

Furthermore, if the maintenance jurisdiction is divided between companies, quick fault location helps to decide who should be responsible for the repair work [1]. These economic and operational benefits emphasize the importance of line fault location. However, fault locator schemes used in AC systems or LCC HVDC schemes may not be directly applicable in VSC HVDC schemes due to differences in the termination, as pointed out in the previous section. Therefore, there is a need to conduct proper investigation to ascertain the limitations of the existing fault location technology when applied in VSC HVDC schemes with long cables or overhead transmission lines and propose solutions to overcome these limitations.

1.4 Objective of the research

The overall research goal is to investigate the use of travelling wave based fault location in VSC HVDC schemes. Fault locator systems already existing for LCC HVDC schemes can be used for VSC HVDC schemes, but the accuracy of detecting travelling wave arrival times need to be improved. Thus, the main focus of the thesis is the investigation of improved measurement techniques for detecting wave front arrival times. To fulfill the research goal following specific objectives are proposed:

- Investigation of the difference between LCC and VSC based HVDC schemes in terms of travelling wave based fault location.
- Development of a method of measurement for detecting travelling wave arrival times in a VSC HVDC scheme.
- Testing and verification of the proposed measurement system through time domain simulation of test networks.

The proposed method of measurement can be validated only through the simulations, as experimentation using a real system is not practical. However, this is not a major limitation since well-established and validated tools exist for power system simulation. This thesis utilizes the well-known electromagnetic transient (EMT) simulation program PSCAD/EMTDC and Matlab software for all the simulations. Since the fault location in cables is more difficult than in overhead transmission lines, most case studies consider a VDC HVDC scheme with a 300 km long DC cable.

1.5 Thesis overview

Chapter 1 includes basic introduction to the thesis, motivation behind the research and the objectives of the research. Chapter 2 presents background information required to understand the thesis. This includes basic Types of faults and expected characteristics of the fault locator and line fault location methods. Travelling wave based fault location method is discussed in detail. Existing fault location technology used in LCC HVDC schemes is described.

Chapter 3 discuss the proposed method to detect fault generated travelling waves and explains how difficult it is to detect travelling waves in VSC HVDC scheme. A technique is proposed to accurately detect the arrival of fault generated travelling waves.

Detailed description of the Rogowski coil modelling is included in the Chapter 4, which is the transducer used to detect the travelling wave. A model of a Rogowski coil suitable for using in EMT programme is developed and verified through experiments.

Simulation results that examine the accuracy of the fault location in a VSC HVDC scheme using the proposed measuring technique are presented in Chapter 5. Sensitivity of the proposed method to various factors is analyzed and improvements are proposed.

Chapter 6 presents conclusions that derived from simulation results and the future work need to be done in this area of research.

Chapter 2

Literature Survey

2.1 Introduction

The literature on fault location of power systems are reviewed in this chapter. Initially types of faults that can occur in power systems are explained. Expected characteristics of the fault locators are described. Then line fault location methods used in power systems are explained with special attention to the travelling wave based fault location method. Subsequently the line fault locators currently used in HVDC systems are discussed.

2.2 Types of faults

Types of faults that can occur in power system are as [1];

- Momentary faults. Also called non-permanent or “transient” faults. This type of faults generally does not call for repairs.
- Sustained faults. Also called “permanent” faults.

- High breakdown faults. Examples: impaired clearance from conductor to ground without actual contact or heavy damage to insulator string.
- Latent faults or insulation weakness. Insulation weakness which does not prevent successful operation under normal conditions but reduces insulation margin provided in design for surges and dynamic overvoltage.

2.3 Expected characteristics of fault locators

A fault locator used on HVDC line/cable should have the following qualities;

- Good accuracy: accuracy must be high, if the line is overhead line, error should be within the distance between two adjacent towers.
- Discrimination: Must be able to discriminate between faults and non-fault conditions.
- Robustness and easy installation: should be able to operate in noisy environment of power lines and not be affected by or affect the mains supply. Equipment must be designed for substation installation and should be simple, rugged, safe, cheap and require low maintenance.

2.4 Line fault location methods

Fault location can be done manually by foot patrols or helicopters with the help of calls from witnesses. But manual fault location is expensive and time consuming when a permanent fault occurs in a long line. There is number of measurement based methods to detect the fault location in a transmission line or cable. These fault location method can be divided in to following main categories [1];

- ❖ Techniques based on impedance measurement.
- ❖ Techniques based on high frequency spectrums of the currents and voltages.
- ❖ Machine learning based approaches.
- ❖ Techniques based on travelling wave phenomena.

2.4.1 Techniques based on impedance measurement

Measuring the impedance of the terminals appears as the simplest way to determine the fault location. Impedance based methods works on phasor values of currents and voltages during the fault to estimate an apparent impedance (or reactance) that is directly associated with the distance to the fault. There are two major categories of line fault location using impedance methods, namely, the single ended method and the double ended method. Two types of single ended methods exist: single-ended methods that use the source impedance and the single-ended methods that do not require the source impedance data [17].

Approach to Impedance based fault location contains following steps:

1. Measure the voltage and currents
2. Extract the fundamental phasors.
3. Determine the fault type.
4. Apply impedance algorithm [17].

Single-ended impedance based fault locators calculate the fault location from the apparent impedance seen when looking into the line from one end. Single-ended impedance methods of fault location are a standard feature in most numerical distance relays. Single-ended impedance methods use a simple algorithm, but susceptible to errors due to arc resistance. Double -ended methods can be more accurate but require data from both terminals. Data must be captured from

both ends before the algorithm to be applied. DC systems cannot adopt this technique directly, because there is no voltage or current phasors in DC systems.

2.4.2 Fault location using frequency spectrums

Techniques based on spectrums of currents and voltages generated by faults are expensive and complex because the use of specially tuned filters. High frequency components of voltage and current after a fault contain information about the fault [18]-[19]. Thus characteristics of the frequency spectrum are used in this method to calculate the fault location [20]. The dominant frequency of the reflected voltage (or current) identified through spectrum analysis can be used to determine the fault location. The method can be explained considering Figure 2-1. If the line is terminated with large surge impedance, the entire incident voltage wave is reflected back towards the line with same sign [18].

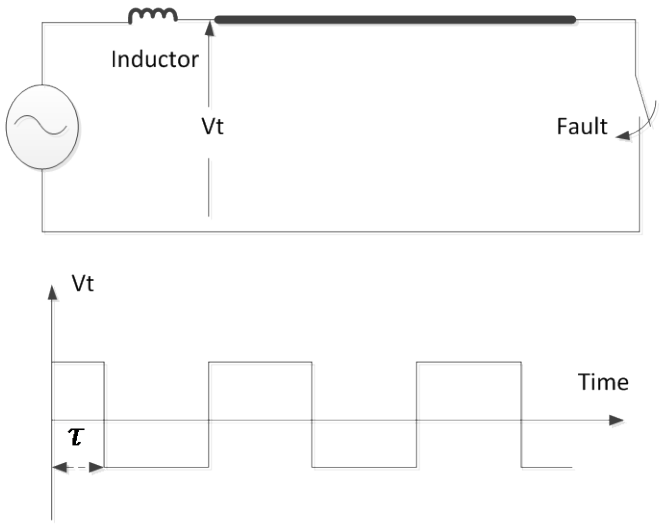

Figure 2-1 Voltage profile of Inductive termination

In Figure 2-1, $\tau$is the propagation time of the surge from the source end to the fault point. The natural frequency (*f*) can be calculated by applying DFT to the voltage waveform measured at the terminal, and it is related to the propagation timeτ as

$$f = \frac{1}{4\tau} \qquad 2\text{-}1$$

The distance to the fault X_F is estimated using the known propagation velocity *u* of the travelling waves as

$$X_F = \frac{u}{4f} \qquad 2\text{-}2$$

This fault location method based on natural frequency of traveling wave does not require identification of wave front arrival times. Thus time tagging of data samples is not necessary since this method is only interested in the frequency spectrum [20]. The fault location results using natural frequency of the surge wave forms will be much better in a DC system when compared to AC system since HVDC system are point to point systems isolated from other natural frequencies due to different network elements. This technique is insensitive to fault type, fault resistance, fault inception angle and system source configuration. However, the reported accuracy of this method is less compared to travelling wave based methods. For HVDC schemes having long cable connections, this method is practically impossible due to attenuation of travelling waves due to high capacitance of the cables.

2.4.3 Machine learning based fault location approaches

Application of knowledge based techniques such as neural networks for fault location has been investigated in the literature. These methods are similar to impedance based fault location

because they are interested in fundamental components of the voltages and currents before, during and after the fault [15]-[16]. The features extracted from the faulty current and voltage signals are fed in to artificial neural network for estimating the fault location. Fuzzy sets are also being used to deal with the uncertainty involved in the process of locating faults in AC networks [16]. This type of fault location methods requires many examples of fault data to train the fault locating system, and the trained system is specific to the system considered.

2.4.4 Travelling wave based fault location

Travelling waves generated by faults travel at a velocity close to the speed of light in overhead lines. In cables the travelling velocity depends on the cable design and the velocity is around half the speed of light. Power systems are large and complex systems, but for steady-state analysis, the wavelength of the sinusoidal currents and voltages is still large compared with the physical dimensions of the network. For 60-Hz power frequency, the wavelength is 5000km. For steady state analysis lumped element representation is adequate for most cases. However, for transient analysis, this is no longer the case and the travel time of the electromagnetic waves has to be taken into account. A lumped representation of, for instance, an overhead transmission line by means of pi-sections does not account for the travel time of the electromagnetic waves. If the travel time of the current and voltage waves is taken into account, the properties of the electric and magnetic field need to be represented by means of distributed capacitances and inductances. An overhead transmission line or an underground cable has certain physical parameters and their inductance, capacitance and resistance is regarded to be equally distributed over their length. After a sudden change in the voltage or current at a point on a transmission line, the gradual

establishment of line voltage and current along the transmission line regarded due to travelling voltage and current waves.

The following section introduces the concepts relevant to wave propagation in transmission lines. The analysis is based on the model of a single-phase lossless distributed-parameter line. The most popular methods for analysis of electromagnetic transients in ideal lines are those developed by Bergeron and Bewley [21]. The Bergeron's method will serve as a basis for the numerical techniques. The method proposed by Bewley, also known as the lattice diagram, will also be explained in this section. Figure 2-2shows the schematic of a single-phase line and the equivalent circuit of a line element.

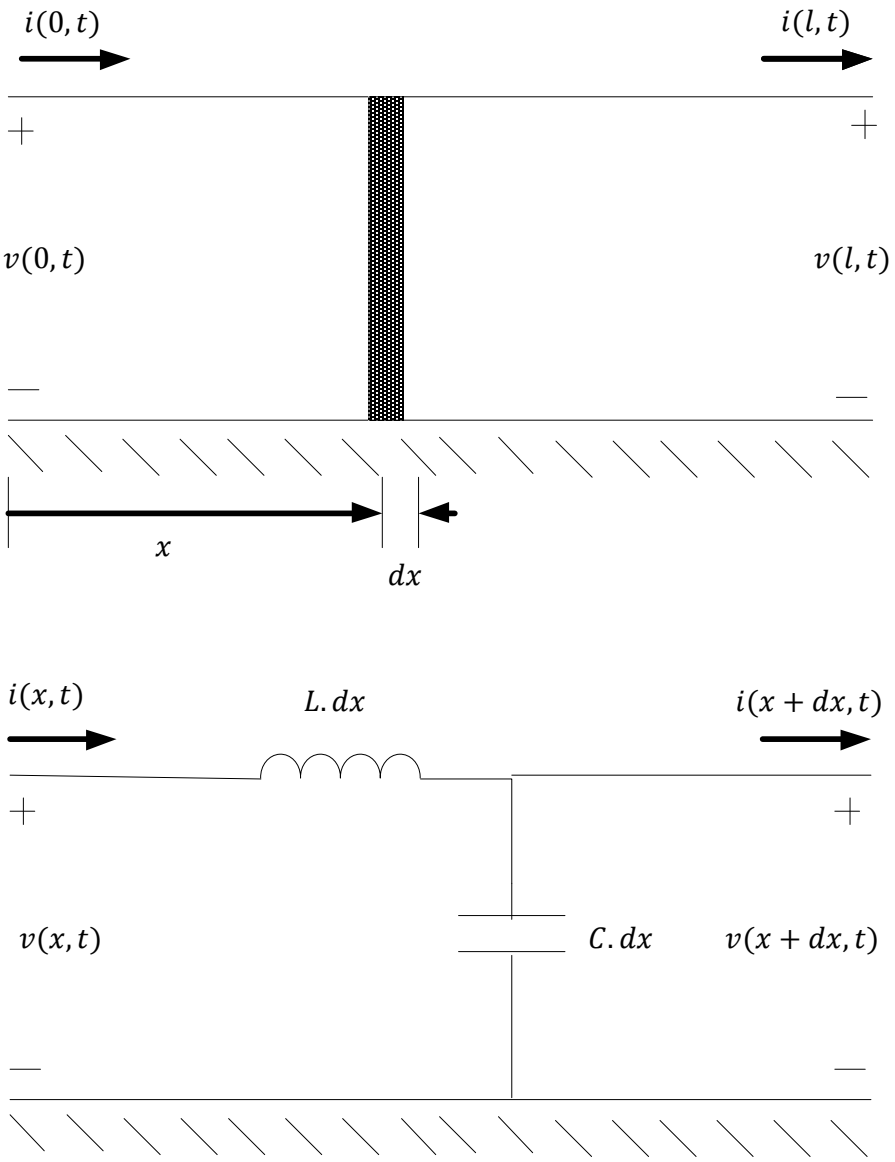

Figure 2-2 Schematic of a single-phase lossless line (top) and equivalent circuit representing an elemental length *dx* of the line (bottom)

The equations for this elemental circuit section can be written as:

$$\frac{\partial\, v(x,t)}{\partial x} = -L\frac{\partial\, i(x,t)}{\partial t} \qquad 2\text{-}3$$

$$\frac{\partial\, i(x,t)}{\partial x} = -C\frac{\partial\, v(x,t)}{\partial t} \qquad 2\text{-}4$$

where L and C are, respectively, the inductance and the capacitance per unit length, and *x* is the distance with respect to the sending end of the line. After differentiating (2-3) with respect the variable *x* and differentiating (2-4) with respect the variable *t*, and equating the expressions for$\frac{\partial^2 i(x,t)}{\partial x.\partial i}$, (2-5)can be obtained. Similarly differentiating (2-3) with respect the variable *t* and differentiating (2-4) with respect the variable *x*, and equating the expressions for $\frac{\partial^2 v(x,t)}{\partial x.\partial i}$, (2-6) can be obtained.

$$\frac{\partial^2 v(x,t)}{\partial x^2} = LC\frac{\partial^2 v(x,t)}{\partial t^2} \qquad 2\text{-}5$$

$$\frac{\partial^2 i(x,t)}{\partial x^2} = LC\frac{\partial^2 i(x,t)}{\partial t^2} \qquad 2\text{-}6$$

The general solution of the voltage equation has the following form:

$$v(x,t) = f(x-\alpha t) + F(x+\alpha t) \qquad 2\text{-}7$$

where $\alpha = 1/\sqrt{LC}$. Both *f* and *F* are voltage functions, and α is the propagation velocity.

Since the current in (2-6) has the same form as the voltage in (2-5), its solution will also have a similar expression. It is, however, possible to obtain a general solution of the current equation based on that for the voltage. This solution could be expressed as:

$$i(x,t) = \frac{f(x-\alpha t) + F(x+\alpha t)}{Z_c} \qquad 2\text{-}8$$

where $Z_c = \sqrt{\frac{L}{C}}$ is the surge impedance of the line.

Note that *f(x – αt)* remains constant if the value of the quantity *(x – αt)* is also constant. That is, the value of this function will be the same for any combination of *x* and *t* such that the above quantity has the same value. The function *f* represents a voltage traveling wave toward increasing *x*, while *F(x + αt)* represents a voltage traveling wave toward decreasing *x*. Both waves are neither distorted nor damped while propagating along the line. The general solution of the voltage and the current at any point along an ideal line is constructed by superposition of waves that travel in both directions. The expressions of *f* and *F* are determined for a specific case from the boundary and the initial conditions.

When a surge travelling along a transmission line reaches a discontinuity point (region where surge impedance is different), part of the incident travelling wave is reflected. The rest is transmitted to the other side. The incident wave, the reflected wave and the transmitted wave are formed in accordance with Kirchhoff's laws. They must also satisfy (2-5) and (2-6).

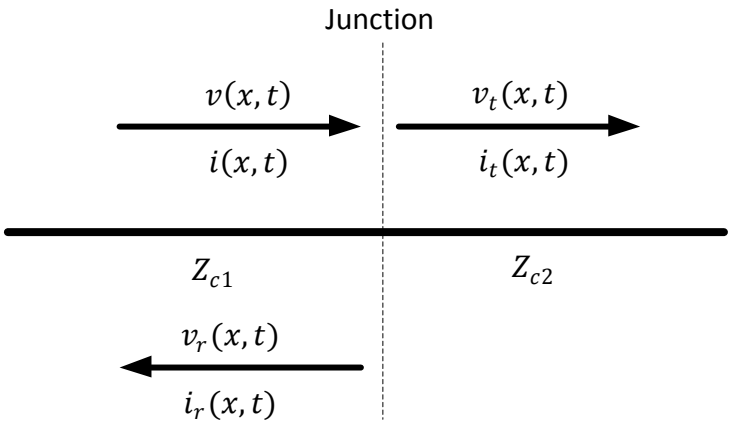

Figure 2-3 Reflection of travelling wave at a junction

The reflected part of the wave is given by:

$$v_r(x,t) = \rho \cdot v(x,t) \quad \text{2-9}$$

$$\rho = \frac{Z_{c2} - Z_{c1}}{Z_{c2} + Z_{c1}} \quad \text{2-10}$$

where ρ is the reflection coefficient, $Zc_1$and Zc_2 are the characteristic impedances of the line segments on either side of the junction (Figure 2-3). Similarly the transmitted part of the wave is given by:

$$v_t(x,t) = \tau \cdot v(x,t) \quad \text{2-11}$$

$$\tau = \frac{2Z_{c2}}{Z_{c2} + Z_{c1}} \quad \text{2-12}$$

where τ is the transmission coefficient. Note that reflections happens only when the surge impedance of two sides are different. Polarity of the reflected wave depends on the magnitudes of the surge impedance values of the two sides. If $Z_{c2} > Z_{c1}$, then the polarity of the reflected voltage will be same as the incident wave. On the other hand, if $Z_{c2} < Z_{c1}$, the polarity of the reflected voltage will be opposite to the incident wave.

The propagation of the travelling waves generated by a fault can be shown on a lattice diagram such as the one shown in Figure 2-4. Figure 2-4 shows the travelling waves initiated due to a fault located at distance X_F away from Converter-1 of a DC line with a total length of *l*. Assume that the waves travel at a constant velocity of *u*.

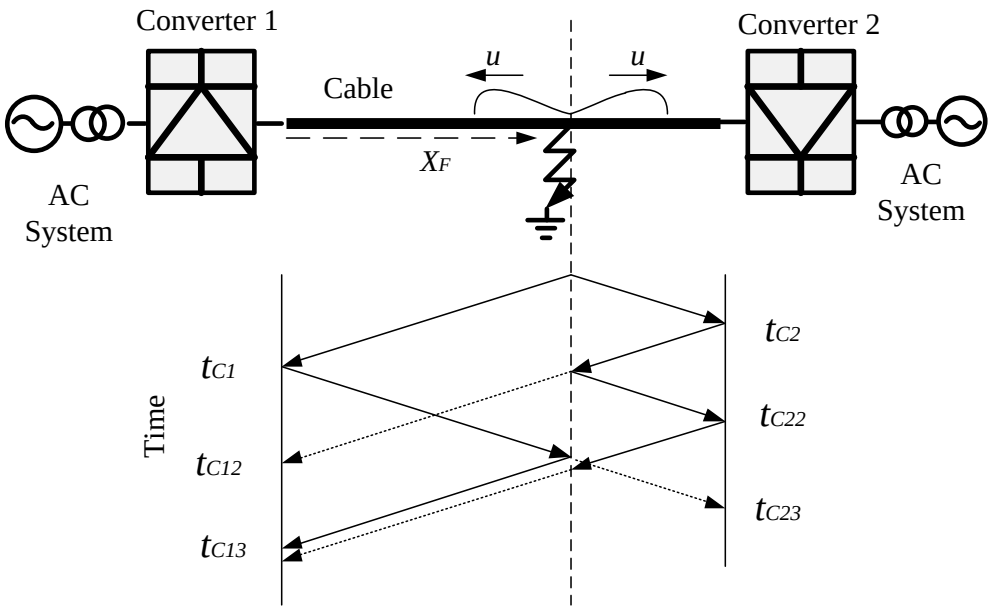

Figure 2-4 Lattice diagram to illustrate the travelling wave flow along the transmission line

Travelling wave based fault location can be either based on measurements at one end or the measurements at both ends [22]. The single ended method requires measurement of the time interval between the arrival of initial and reflected waves at a terminal. DC line fault location can be calculated using the travelling wave arrival time with respect to a single terminal (for example Converter-1 in Figure 2-4). This method is also called Type A method [1].

The more reliable two ended method requires measurement of the time interval between the arrivals of initial waves at two ends, thus needing synchronization of the measurements at the two terminals. Availability of Global Positioning System (GPS) and hardware that enables collecting time tagged data samples at very high frequencies allows development of highly reliable and accurate fault location schemes [2]. In the double ended method, the fault location is found by (2-13) using the initial travelling wave arrival time at both the terminals. This method is called double-ended method or Type D method [1].

$$X_F = \frac{l - u \cdot (t_{C2} - t_{C1})}{2} \qquad 2\text{-}13$$

In the single-ended method the analysis of the waveforms has to be more sophisticated [23]. As an example consider the case shown in Figure 2-4, where the fault location X_F is greater than $l/2$. The reflected wave from the Converter-2 terminal arrives at time: t_{C12}, before the second reflection arrives at time: t_{C13}. Therefore, signature analysis may be required to distinguish the two waveforms [23]. The double-ended method is based on timings from the initial surges and hence the reflected waves are not involved. However, double-ended method requires both an accurate method of time synchronization and an easy means of brining the measurements from the two terminals to a common point. GPS provides time synchronization accuracies of 1μs[2]. Since the fault location calculation does not have to be 'real-time', data can be exchanged using the communication channels installed for HVDC converter control.

2.5 Current LFL technology

Impedance based fault location cannot be directly employed in DC systems because the impedance is essentially resistance of the DC line and it is small and causes large errors due to fault resistance. Even though there are no practical instances where the high frequency methods are being used to calculate the fault location, literature can be found on this topic [20]. As mentioned before, the accuracy of this method less than travelling wave based fault location.

Travelling wave based fault locators use time tagged samples of voltages or currents to calculate the fault location. It is highly dependent on accurate detection of travelling waves, and therefore on the accuracy of time tagging of each and every sample. Travelling wave based fault location is employed in both AC and DC power systems but when employed in AC systems there is a

possibility of not generating travelling waves if the fault occurs at an instant when the voltage is close to zero. This can result in inaccuracies in the fault location. In DC systems this is not a problem because the voltage magnitude is always a high value. This makes DC lines an ideal place to apply travelling wave based fault location. Almost all the line fault locators in DC systems use the travelling wave based fault location techniques.

Two main factors considered when selecting a travelling wave based fault location scheme are the cost of installation and the accuracy of fault location. Although calculations involved in travelling wave based fault location schemes are simple in theory, their implementation is challenging due to various factors that contribute to errors. These include bandwidth limitations of transducers, A/D conversion and sampling precision, synchronization errors, wave front detection algorithm errors and the propagation velocity deviations due to changes in physical parameters, especially in cables [2]. To increase the accuracy of the fault location scheme, improvement of every factor mentioned above is necessary. The quantization errors are due to limited bit resolution and the sampling errors are due to low sampling frequency of the A/D conversion electronics. With the advancement of technology, data acquisition (DAQ) hardware with A/D conversion resolutions as high as 16 bits at megahertz range sampling frequencies has become available at reasonable costs. Propagation velocity deviations are mainly due to temperature variations and aging effect of the cables and should be compensated if possible.

If travelling wave based fault location is used to locate a fault in power system, the signal observed in order to determine the travelling wave arrival time varies depending on the power system. In HVAC schemes current and voltage waveforms are sinusoidal and fault generated travelling wave is superimposed on it [7]. In HVDC schemes, the current and voltage waveforms are predominantly of 0 Hz and the lines are terminated with a large capacitor or inductor

depending on the HVDC technology used. The smoothing reactors used in LCC HVDC schemes cause a large voltage spike at the line/cable terminal when a travelling wave arrives. The large DC capacitor in VSC HVDC schemes appear as an ideal voltage source to the line/cable and therefore, a sharp transient voltage will not appear at the cable/line terminal. Most of the existing HVDC line fault locators are designed for traditional line commutated convertor (LCCs) based HVDC schemes. However, differences in the termination of the cable/line between LCC and VSC based HVDC schemes that may impact accuracy of fault location.

After an occurrence of fault, voltage and current travelling waves starts to propagate along the line/cable away from the fault point. When both voltage and current travelling waves arrive at a termination station, part of the incident travelling wave is reflected back towards the fault and part is transmitted towards the converter. The reflection coefficient at the converter station depends on the termination circuit but reflection coefficients of voltage and current always remains opposite for any termination circuit [25]. Although, the capacitive termination in VSC schemes does not allow sharp changes in voltage at the terminal, it allows sharp changes in the observed current when the current waves reaches the terminal. Similarly, the inductive termination in LCC converters does not allow sharp transient changes in the current. In LCC HVDC systems surge capacitors are installed at the terminals to suppress the high voltage surges entering into the converter. Voltage change caused by the travelling wave generates current proportional to the rate of change of voltage through the surge capacitor. So the travelling wave can be detected by placing a current transformer (CT) on the earth wire of the surge capacitor.

Chapter 3

Surge Detection Method

3.1 Introduction

Measurement method and transducers need to be selected in such a way that it satisfies necessary requirements by the application. Accurate detection of travelling wave (either voltage or current) arrival times is important for locating the fault accurately. It is apparent from (2-13) that fault location accuracy is directly related to the accuracy of measuring the time difference between the arrivals of fault initiated voltage (or current) waves at the two terminals. Since the velocity of travelling waves in overhead lines is close to the speed of light, a one microsecond error in time difference measurement will translate into approximately 300 m error in the estimated fault location. In travelling wave based fault location, the focus is to measure the surge arrival times as accurately as possible rather than accurately measuring the magnitudes of the waves. This is because the fault location (2-13) needs just the surge arrival time. Since the travelling waves are transients with a very fast rise time, the transducers used for measurements need high bandwidth and fast slew rate.

3.2 Sensors for measuring transient signals

One of the major issues that arise when measuring transient signals is the bandwidth and slew rate limitations of the transducers. Noise in the measurements could also become a problem especially in substation environments with strong electric and magnetic fields. Inaccuracies in the measurement will result in errors in the fault location calculation. Safety is another concern and the transducer secondary should be properly isolated from the high voltages so that they can be safely connected to low voltage computer based equipment. Furthermore, the transducers must be cost effective and should occupy a small physical space in a substation. A few sensing technologies available are briefly discussed below.

3.2.1 Coaxial shunts

Coaxial shunts can be used to measure currents ranging from amperes to kilo amperes. It offers several advantages like relatively high output voltage, low input impedance, unaffected by stray fields and high bandwidth ranging from DC to megahertz. Disadvantage of coaxial shunts is it needs to be directly connected to primary circuit and must be mounted at ground potential.

3.2.2 Current transformers

Standard current transformers (CT) have a limited bandwidth (up to 100 kHz [26]). The eddy current losses in the magnetic core increase with the frequency and that limits the high frequency components of the current from being measured. The resonance between the inductance of the

CT and the stray capacitance of the winding determines the cut off frequency. Low frequency currents cannot be measured correctly because of the core saturation of CT. Use of large magnetic cores improves the frequency characteristics of the CT but it results in more than the proportional increase of price.

3.2.3 Hall effect sensors

When a current-carrying conductor is placed in a magnetic field, a voltage will be generated in a direction perpendicular to both the current and the field. This principle is known as the Hall effect. The Hall effect sensor is a magnetic field sensor based on the Hall effect. It is an isolated, non-intrusive device that can be applied to both DC and AC current sensing, with a bandwidth up to several MHz. Due to its simple structure, compatibility with the microelectronic devices, a Hall effect current sensor device can be monolithically integrated into a fully integrated magnetic sensor[27][28]. However, it is usually more costly than a current transformer or a Rogowski sensor. In addition, it is very sensitive to external magnetic fields. Hall Effect sensor may not be suitable for transient detection in HVDC schemes due to its inability to work under high external magnetic fields.

3.2.4 Rogowski coils

The output of a Rogowski coil is proportional to the rate of change of current [29]. Thus it will produce a zero output when measuring DC currents and non-zero output during transients. In normal applications, a suitable integrator is connected to the output of the Rogowski coil to derive an output voltage proportional to the measured current. However, in transient detection

this integration stage is not necessary. In fact it is advantageous to measure rate of change of current than current. Therefore, the Rogowski coil is an ideal current transducer for detecting transient currents. It gives isolated current measurements, does not saturate with high currents, and has an excellent bandwidth comparable with other current transducers.

3.2.5 Voltage dividers

A voltage divider generates a measurement signal proportional to the high voltage being measured but of a considerable smaller magnitude at ground potential. Voltage dividers are built with combinations of resistive and capacitive elements. Capacitors do reduce the bandwidth of the voltage divider making it impossible to use for travelling wave based fault location due to its limited bandwidth.

3.3 Signals available for travelling wave detection

The terminal voltages and currents are the most obvious signals for detection of the arrival of travelling waves. However, there are additional signals that may be utilized for this purpose depending on the terminal configuration. In LCC HVDC systems usually have surge capacitors installed at the line terminals to suppress the high voltage surges travelling into the converter. Surge capacitors are connected between the line terminal and the ground, and typically in the range of tens of nano-Farads. Voltage change caused by the travelling wave generates a current proportional to the rate of change of voltage through the surge capacitor. Therefore, travelling waves can be detected by placing a current transducer on the earth wire of the surge capacitor [30].

Transmission and reflection of a travelling wave is dependent on surge impedances of both sides. Detailed explanation of this phenomenon was given in Chapter 2. Termination of LCC HVDC and VSC HVDC technologies are different due to their inherent properties. Because of the large series connected smoothing inductor, an LCC has large termination impedance while a VSC has low termination impedance due to large parallel connected DC capacitor. Therefore, the same travelling wave would produce different terminal voltage variations in the cases of LCC and VSC HVDC systems. The effect of cable or transmission line termination on the measured terminal voltage and/or current can be analyzed as follows.

Consider Figure 2-2, and assume that the incident wave can be represented by

$$v(x,t) = Ae^{-(x-\alpha t)} \quad 3\text{-}1$$

As described earlier, the reflected and transmitted components can be represented as

$$v_r(x,t) = \rho \cdot \left(Ae^{-(x-\alpha t)}\right) \quad 3\text{-}2$$

$$v_t(x,t) = \tau \cdot \left(Ae^{-(x-\alpha t)}\right) \quad 3\text{-}3$$

The voltage variation observed on the incoming branch at the junction is therefore:

$$v_o(x_o,t) = v(x_o,t) + v_r(x_o,t) \quad 3\text{-}4$$

$$v_o(x_o,t) = (1+\rho) \cdot \left(Ae^{-(x_o-\alpha t)}\right) \quad 3\text{-}5$$

$$v_o(x_o,t) = (1+\rho) \cdot v(x_o,t) \quad 3\text{-}6$$

$v_o(x_o,t)$is the observed voltage at distance x_o. The value of ρ is between -1 and +1 depending on values of $Z_{c1}$and Z_{c2}. Therefore, $0 < (1+\rho) < 2$. When the cable or transmission line is terminated by an inductor, the surge impedance of the termination is:

$$Z_c = \sqrt{\frac{L}{C}} \rightarrow \infty \quad 3\text{-}7$$

On the other hand, when the cable or transmission line is terminated by a capacitor, the surge impedance of the termination is:

$$Z_c = \sqrt{\frac{L}{C}} \rightarrow 0 \qquad 3\text{-}8$$

For capacitive termination, such as at the terminal of a VSC HVDC, ρ is close to -1 and (1+ρ) is close to zero. This will significantly reduce the magnitude of the observed waveform as illustrated in Figure 3-1.

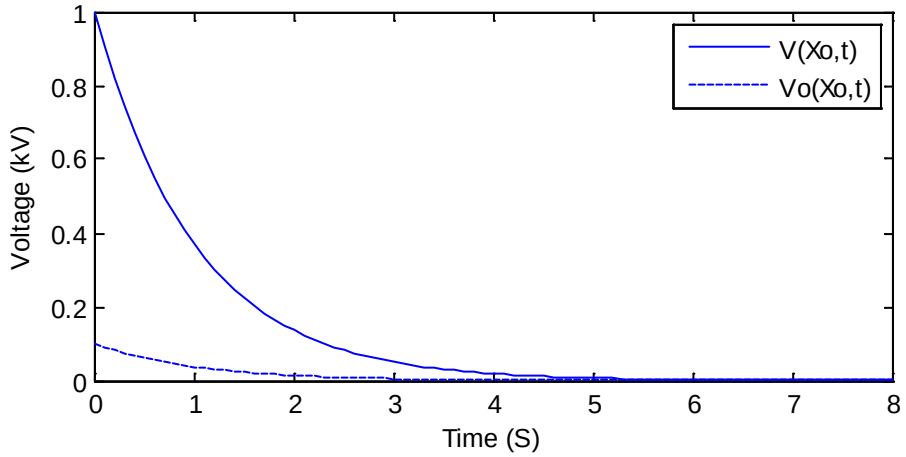

Figure 3-1 Voltage travelling wave $v(x_o, t)$ arriving at a capacitively terminated end of a line and the voltage observed at the terminal $v_o(x_o, t)$

At the terminal of an LCC HVDC scheme, the voltage wave reflects with the same polarity since the surge impedance of the line is less than the surge impedance at the terminal. This condition is generally satisfied due to large smoothing reactor at the converter DC terminal, and therefore a larger transient voltage is observed.

Although series inductors are not required for the normal function of VSC HVDC systems, often a small series inductor is connected at the converter terminals to protect IGBTs from large rates

of change of currents during DC side faults. However, there is no published literature that indicates the methods of calculation of this inductance or typical values. After consulting various experts, it was found that a series inductance of 10 mH would be reasonable at the terminals of the cables or transmission lines. If there are no series inductors at the terminals, detection of travelling waves based on voltage waves is impossible for VSC HVDC schemes having long cables or overhead lines. If there are no series inductors installed in the VSC HVDC scheme, it could be economical to include a small series inductance at the cable termination specifically for the purpose of traveling wave detection.

3.4 Analysis of wave front detection

As mentioned earlier, arrival of travelling waves can be detected by measuring the terminal voltage, terminal current or the surge capacitor currents. Surge capacitor current is the method used in existing fault locators designed for LCC HVDC schemes. One attractive feature of the surge capacitor current is that it can be measured close to the grounding point. Therefore the sensor insulation requirements are minimal and the measurement system is at the ground potential. This makes the instrumentation simpler, safer, and cheaper. Moreover, the current through the capacitor at steady state is zero, and the current resulting from the arrival of a wave is proportional the rate of change of voltage of the voltage wave. This makes the transients in the surge capacitor current sharper than the original wave front. However, there is a question whether this arrangement would work in the case of VSC HVDC schemes. If a Rogowski coil (without integrator) is used to measure the surge capacitor current, its output voltage is approximately proportional to rate of change of surge capacitor current, and therefore, to the

second derivative of the voltage wave. As a result on arrival of a travelling wave, the sensor (Rogowski coil) output will show a transient sharper than the surge capacitor current itself.

To compare different options, the test system shown in Figure 3-2. Figure 3-2 is simulated in PSCAD/EMTDC. Simulation model of VSC HVDC scheme is rated at 200 MW with a rated voltage of 400 kV (pole to pole). At the Converter-1 side VSC HVDC scheme is connected to a 400 kV AC network represented by its Thevenin's equivalent circuit (impedance of $26.45\angle 80°\Omega$ and a voltage of 420 kV). At the Converter-2 end VSC HVDC scheme is connected to an AC network having the same Thevenin's equivalent circuit as in the rectifier side. Frequency at the rectifier end is 60 Hz and the frequency at the inverter end is 50 Hz. Main parameters for the 300 km long cable system are shown in Figure 3-3. Core conductor of the cable is solid and there are two other conducting layers. In between the conducting parts three insulation layers are provided. Frequency dependent phase model of the transmission cable was used for the simulations. Although there is no inherent need for series inductors, it is assumed that there is a small series inductor to limit the rate of change of current entering the converter during the DC faults. Thus a possible arrangement for wave front arrival time detection is to use the output voltage of a Rogowski coil measuring the surge capacitor current. Such a scheme is schematically shown in Figure 3-4. Time step used for the simulations is 0.5 μs.

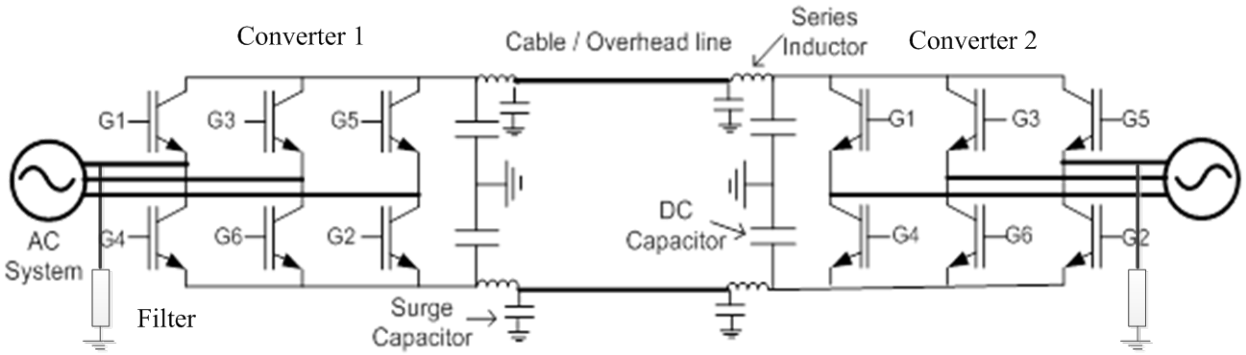

Figure 3-2 Test system used for the simulations

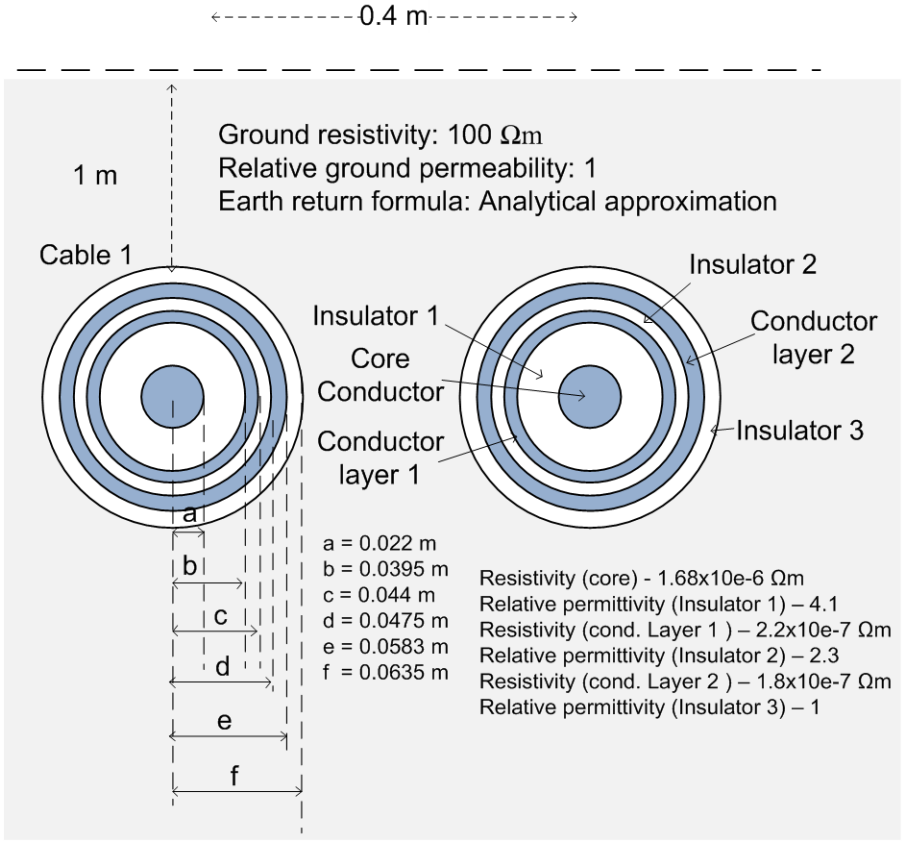

Figure 3-3 Parameters of the cable

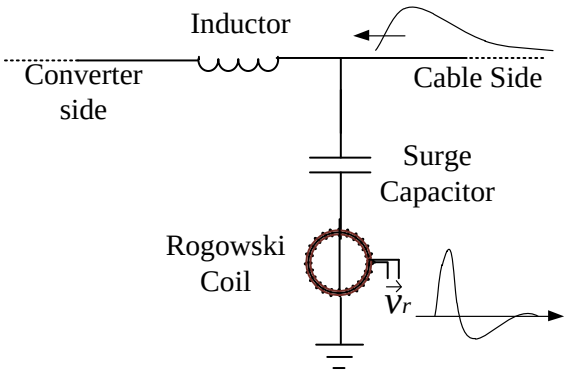

Figure 3-4 Proposed termination

The following observations are presented here are for a solid pole-to-ground (P-G) fault 70 km away from Converter-1 of the VSC HVDC scheme. The fault is applied at 0.6 S. Figure 3-5 shows voltage waveform observed at Converter-1 terminal subsequent to this fault. From Figure 3-5b it is obvious from that determination of the exact time of arrival of the wave is quite challenging using this gradually changing waveform.

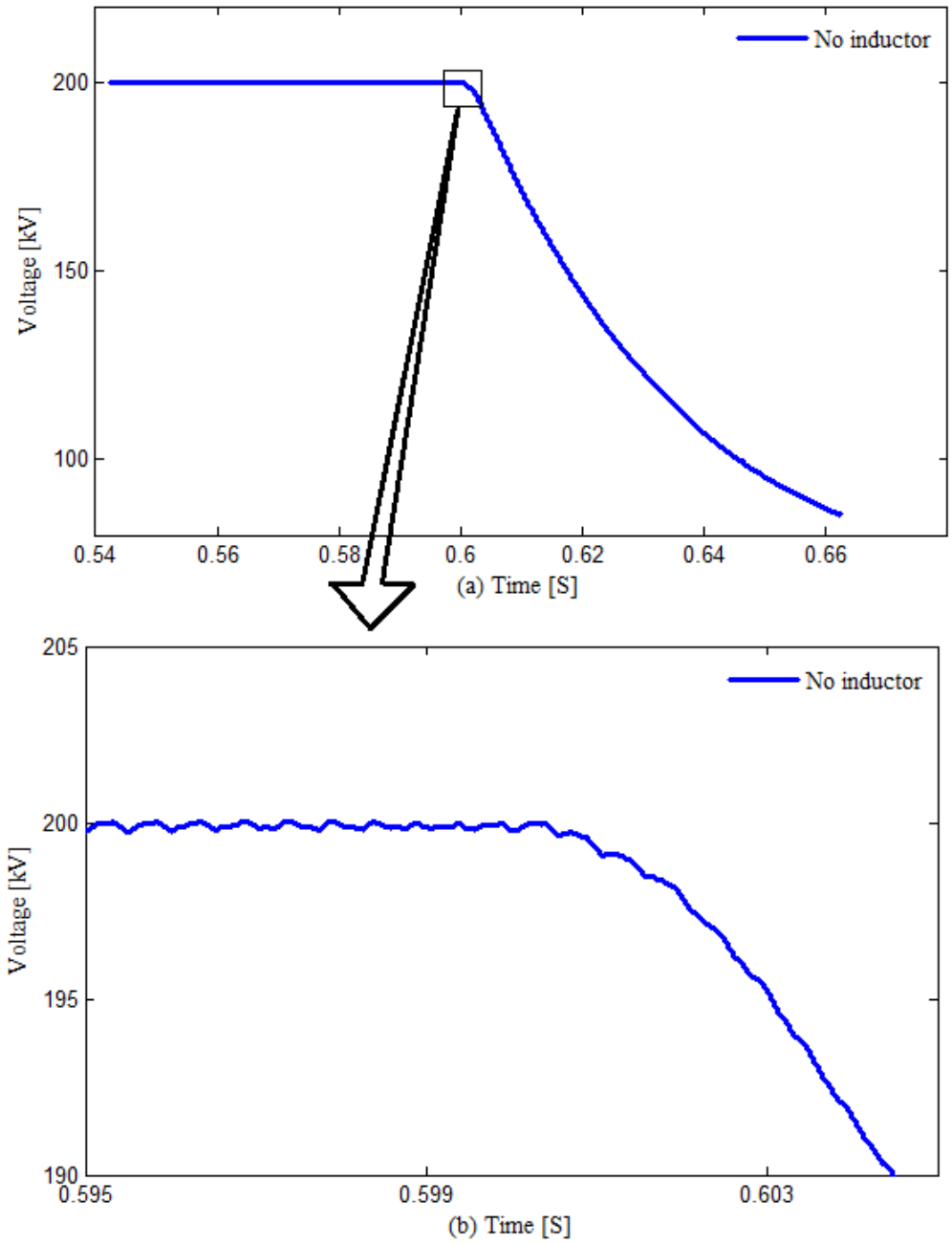

Figure 3-5(a) Cable terminal voltage variation for a solid P-G fault 70 km away from Converter-1 (b) Zoomed view

However, inclusion of a small series inductor between the DC capacitors and the cable termination changes the situation considerably. Figure 3-6 compares the terminal voltage variations for the same DC fault, with and without a small series inductor. A clearly distinguishable voltage spike is produced when there is a series inductor. It was observed that even for 1 mH series inductance, a sharp change in the voltage waveform is observed when a fault generated travelling wave arrives at the terminal.

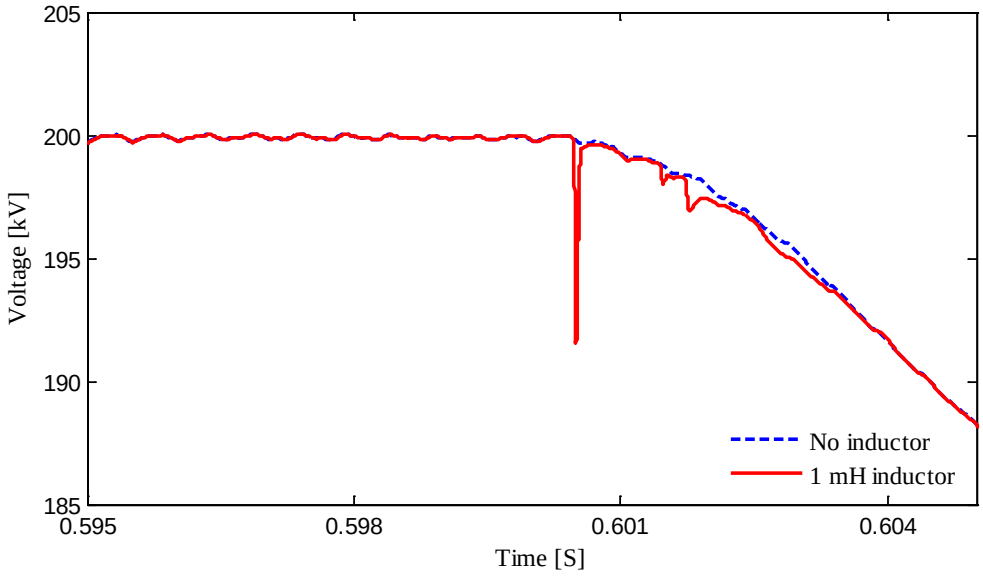

Figure 3-6 Terminal voltage waveforms with and without a series inductor for a solid P-G fault 70 km away from Converter-1.

In contrast, line current shows a sharp change when the fault generated current waves arrive at the converter terminal. Figure 3-7 compares the terminal current variation before and after inclusion of the series inductor. As expected, the sharpness of the current transient has reduced when the inductor is included in the current path. Use of current as an input signal is not convenient because:

- ❖ Transducers need to be installed at very high potentials. This will make the fault locator expensive and bulky.
- ❖ Electrical isolation is needed between sensor output signal and the data acquisition system.

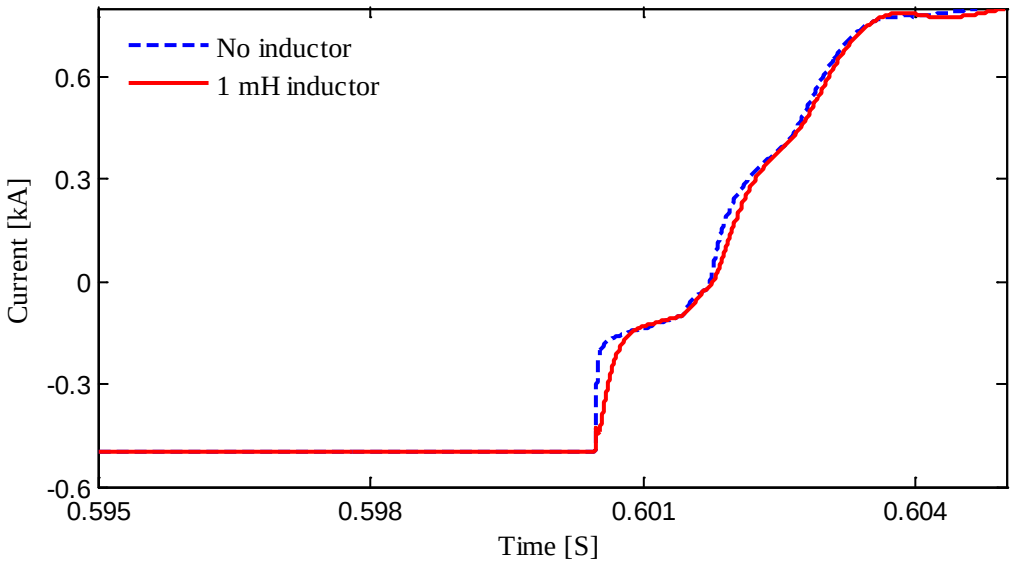

Figure 3-7 Terminal current variation with and without a series inductor (1 mH) for a solid P-G fault 70 km away from Converter-1

Figure 3-8 shows the variations of the surge capacitor (100nF) current for the same fault, for the cases of with and without 1 mH series inductor. Note that without the series inductor, surge capacitor currents are useless for detection of travelling waves, but when the series inductor is connected, surge capacitor current produces a sharp transient change making it ideal for detecting the arrival of travelling wave fronts. Figure 3-9 shows the same comparison when the series inductor is 10 mH. Increasing of the inductance does not proportionately increase the

magnitude of the transient current. This indicates that presence of inductance as small as 1 mH would enable detection of travelling waves using surge capacitor currents.

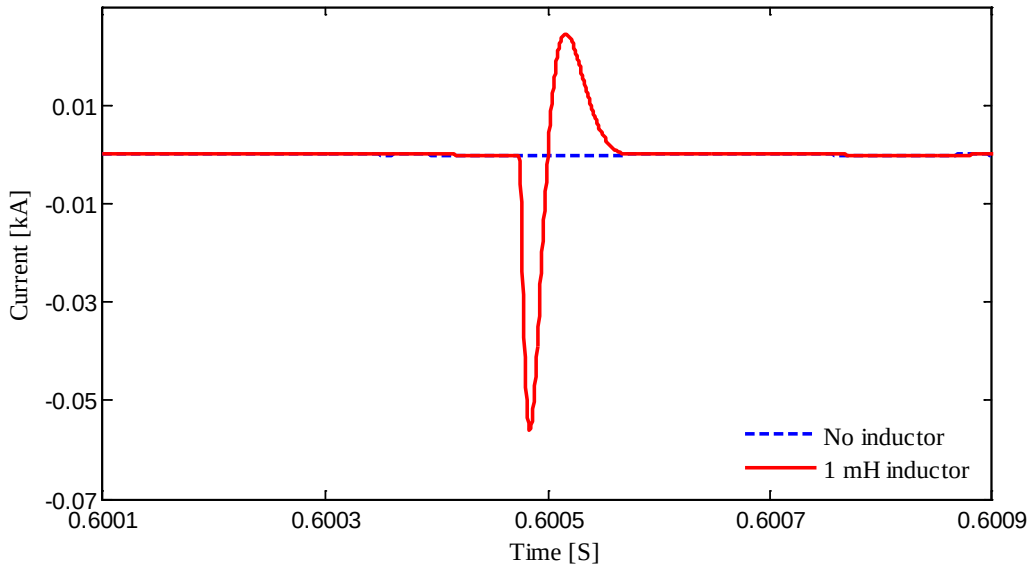

Figure 3-8 Surge capacitor current variation with and without a series inductor (1 mH) for a solid P-G fault 70 km away from Converter-1

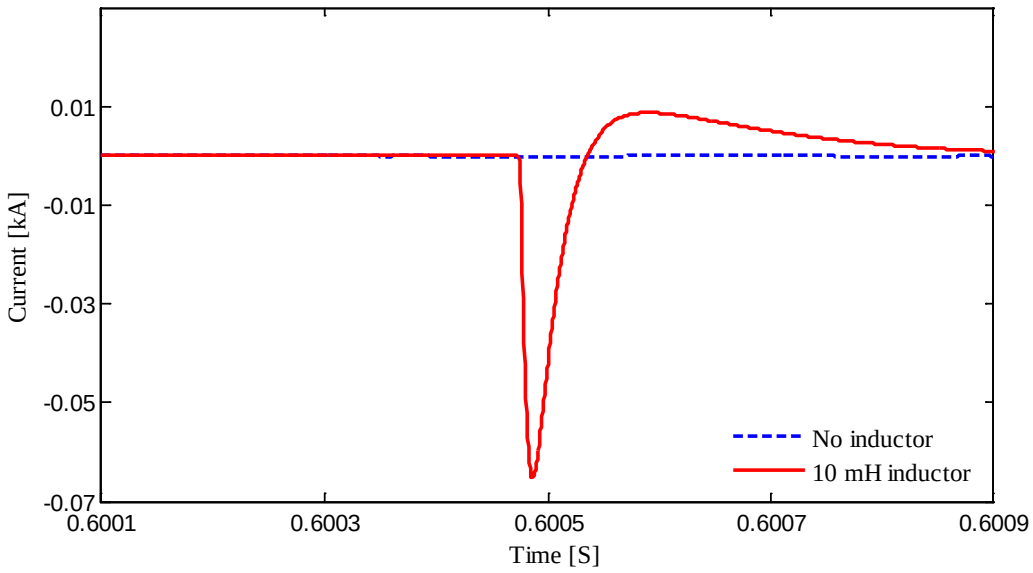

Figure 3-9 Surge capacitor current variation with and without a series inductor (10 mH) for a solid P-G fault 70 km away from Converter-1.

Figure 3-10 shows rate of change of surge capacitor currents with several different series inductor values for the same fault considered earlier. The rate of change of surge capacitor current waveform has a sharper transient change than that observed in the original surge capacitor current. Since a Rogowski coil has an output voltage approximately proportional to rate of change of current flowing through it, if a Rogowski coil is used to measure the surge capacitor current, its output voltages signal should have the same shape as those shown in Figure 3-10. Also, the sensitivity of the rate of change of surge capacitor current waveform peak magnitude to the series inductance used is minimal if the inductance is larger than 1 mH. The peak of the observed signal starts to drop when the inductance is less than1 mH. From these observations, it can be concluded that a very small inductance such as 1 mH in series with the cable give rise to a sharp terminal voltage change, and hence a sharp surge capacitor current. If a Rogowski coil is used to measure this surge capacitor current, its output voltage can conveniently be used to detect the arrival time of the travelling waves.

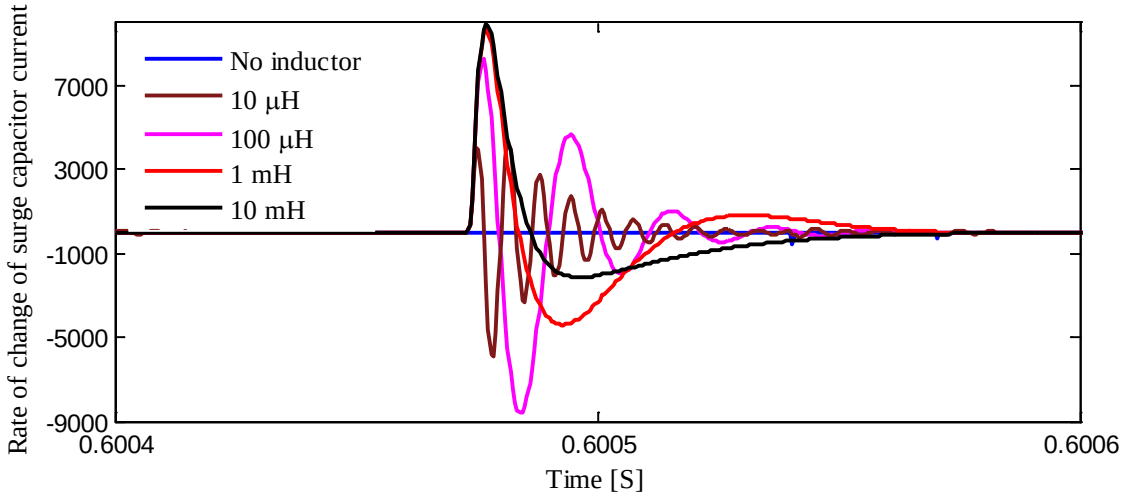

Figure 3-10 Variation of the rate of change of the surge capacitor current for a solid P-G fault 70 km away from Converter-1 (surge capacitance fixed at 100 nF)

Sensitivity of the peak value of the observed rate of change of surge capacitor current signal to the surge capacitance was also investigated and the results are shown in Figure 3-11. The results in Figure 3-11 were obtained with a fixed series inductance of 1 mH. As expected the peak of the signal increases with the size of the surge capacitor, however, the peak value of the signal was not doubled when the capacitance was changed from 50 nF to 100 nF (or from 100 nF to 200 nF). Generally, larger the surge capacitor, better the detection signal will be. However, in modern HVDC system, tendency is use smaller surge capacitors in the range of several tens of nano farads.

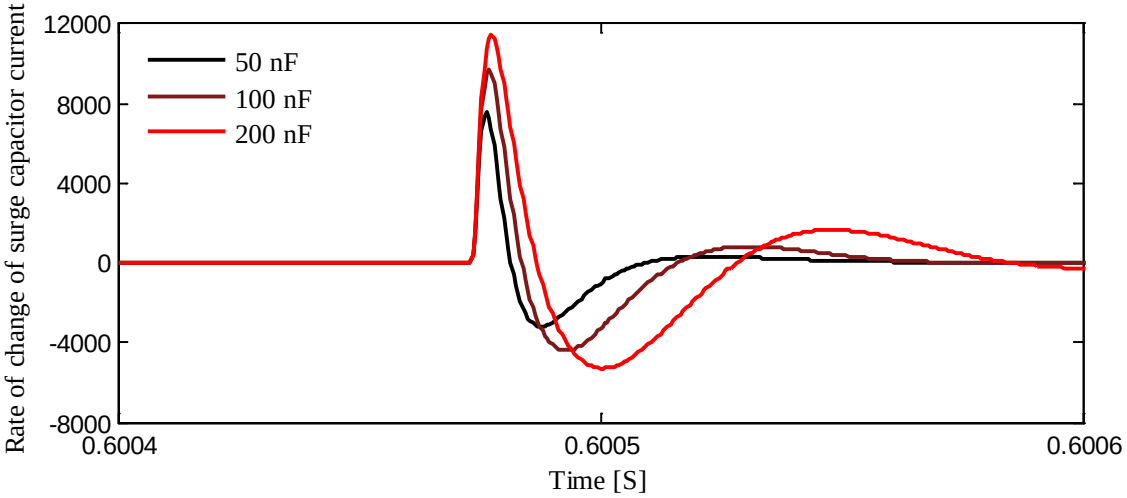

Figure 3-11 Variation of the rate of change of the surge capacitor current for a solid P-G fault 70 km away from Converter-1(series inductance fixed at 1 mH)

3.5 Experimental results

Although simulations indicate this is a good strategy for detecting travelling waves in VSC HVDC systems, feasibility of the measurement system under real conditions was a question. This is especially because the output voltage of Rogowski coils could be small (few mV) and the noise in a substation environment could be detrimental to the measurements. In order to understand the situation, an experimental measurement was conducted at Nelson river HVDC system located in Manitoba, Canada. Nelson River HVDC system is an LCC system and consists of two bipoles. Two rectifier stations located in Radisson and Henday are connected to the inverter station located in Dorsey (near Winnipeg, Manitoba, Canada) via two overhead lines (895 km and 937 km long). Bipole-1 can transfer up to 1620 MW of power at ± 450 kV, while Bipole-2 has a rating of 1800 MW at ±500 kV. Both bipoles share the same right of way (ROW) for transmission.

A commercial Rogowski coil was installed on one of the surge capacitor (55 nF) grounding circuits in Dorsey converter station. The termination circuit at the Dorsey converter station was similar to that was shown in Figure 3-12. The parameters of the Rogowski coil used for the experiment are listed in Table 3-1. The data were recorded at 2 MHz sampling rate using a 16-bit D/A converter during the summer of 2011. A sample of the recorded waveforms is shown in Figure 3-13. The recorded Rogowski coil voltage has a very sharp transient similar to those observed in the simulations. The signal peak is cut-off due to saturation. Contrary to the expectation, the signal has a very low noise level. The zoomed portion of the signal shown in Figure 3-13b shows that noise is in the range of ±4 mV. Although Nelson River HVDC schemes is an LCC based scheme with a large series inductor, the experimental measurements provide

good indication of the signal and noise levels that can be expected under actual conditions. This is the most important insight obtained through the experimental measurements. In addition to that, the actual measurements also indicate the general accuracy of the shape of simulated waveforms.

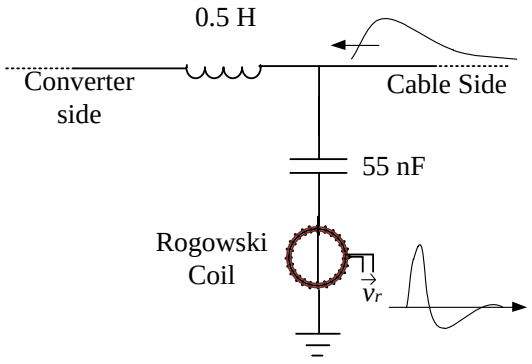

Figure 3-12 Termination of the overhead line at Dorsey converter station

Table 3-1 Parameters of the Rogowski coil used for the experiment in Dorsey converter station

Inner radius	260 mm
Outer radius	284 mm
Resistance	468 Ω
Self-Inductance	3.5 mH
Capacitance	60.93 pF
Mutual-Inductance	0.55 μH

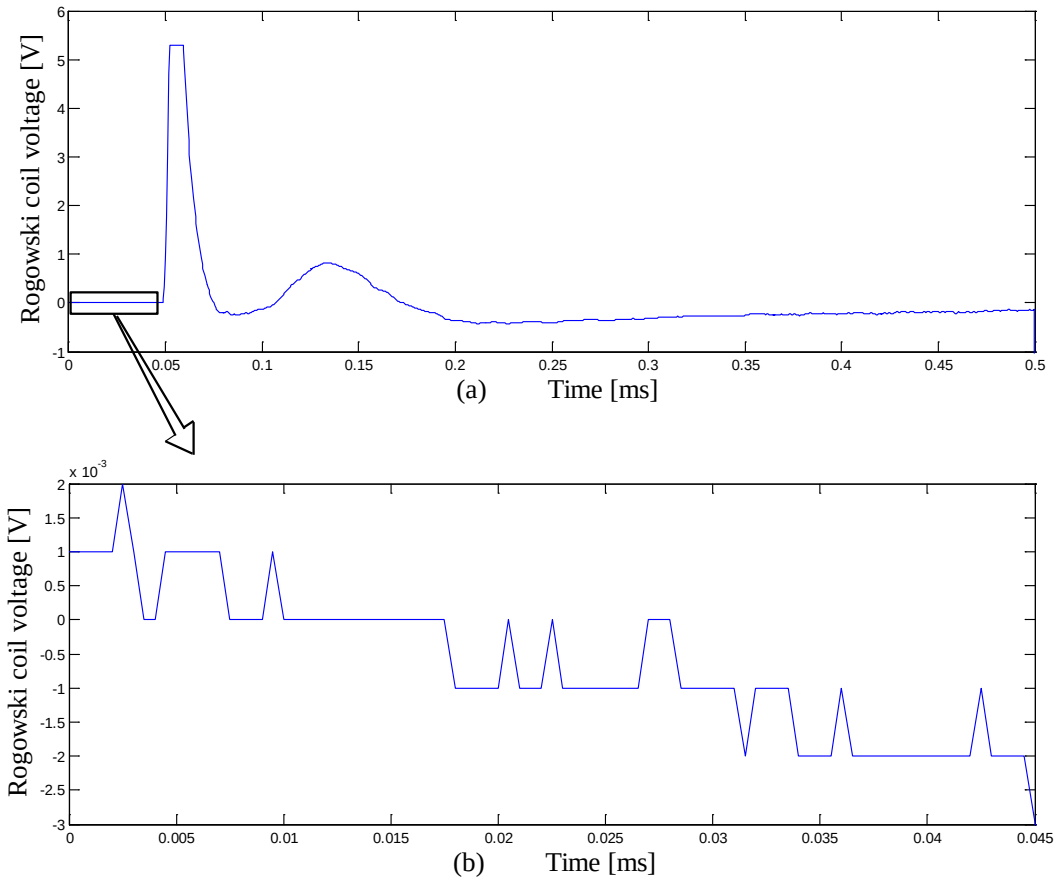

Figure 3-13(a) Rogowski coil voltage for a fault 356 km away from Dorsey converter station (b) Zoomed view indicating the noise level.

3.6 Concluding remarks

Simulations show that the voltage travelling waves cannot be detected at the terminal of a VSC with reasonable accuracy, if there is no series inductor. However, presence of even a small series inductance allows voltage travelling waves to be observable. The value of the series inductor is not that important as long as it is above 1 mH. Since the current flowing through the surge capacitor is proportional to the derivate of the voltage across the capacitor, much sharp change in

the surge capacitor current can be observed. The derivate of the surge capacitor current signal produces even sharper transient change. Thus measuring the surge capacitor current using a Rogowski coil is a good method for detecting the travelling wave arrival times. In order to understand the behaviour of the Rogowski coil in HVDC converter station Experimental measurements carried out in Dorsey HVDC converter station of Nelson River HVDC scheme. Experiments carried out confirmed that the Rogowski coil output has desired characterises required to be used as input signals to a HVDC line fault locator. In order to properly investigate the applicability of the Rogowski coils under verity of situation, a model of the Rogowski coil suitable for simulation studies must be developed and validated. The next chapter describes the development and verification of such a simulation model.

Chapter 4

Modelling of Rogowski Coil

4.1 Introduction

A Rogowski coil consists of helical coil of wire with the wire from one end returning through the center of the coil to the other end, so that both terminals are at the same end of the coil. When the coil is placed around a conductor which carries the current to be measured, it generates a voltage proportional to the rate of change of current in the encircled conductor. Rogowski coils offer many benefits over traditional iron core transformers (CTs) which have a rigid mechanical design and often subjected to magnetic saturation. Large and heavy CTs are needed when measuring large currents and several CTs may be needed if the range of the measured current is varying over a wide range. In contrast, flexible Rogowski coils allow measurements to be taken in spaces inaccessible to traditional iron core CTs. Wider measuring range of Rogowski coils eliminates the need for several CTs for the same measurement. Furthermore, because of its low output voltage, Rogowski coils eliminate hazards like inductive kick due to accidental opening of CT secondaries [31]-[35].

In order to simulate the complete travelling wave detection system, it is necessary to implement a model of a Rogowski coil in PSCAD/EMTDC, the electromagnetic transient simulation program used in this research. Rogowski coil theory is based on Ampere's and Faraday's laws, and it provides a beautiful demonstration of the above mentioned laws. Because of inherent linearity of Rogowski coil, the response of the coil under extreme measuring conditions is much closer to the theoretical explanations than iron cored measuring instruments [34]. However, when modeling a Rogowski coil used in a high frequency application such as fault generated surge measurement, effects of its self-inductance and capacitance need to be properly represented.

4.2 Rogowski coil models

Consider the Rogowski coil shown in Figure 4-1, with N_s number of turns, a circular cross-section area of A m^2, and a length of l m. Often, the winding at one end of a Rogowski coil returns along the length of the coil through a conductor along the axis of the coil. This arrangement reduces pick-up of external magnetic interference, and conveniently ensures that the connections to the coil are both at the same end. The Rogowski coil is placed around the conductor that carries the current to be measured. A change in the primary current will induce a voltage across terminals of the coil.

If a loop is drawn through the center of Rogowski coil, according to the Ampere's law line integral of magnetic field along the loop is equal to the current enclosed by the loop. From that relationship, an expression for the magnetic field can be obtained irrespective of the shape of the loop.

$$\oint H(t) \cdot \cos(\alpha) \cdot dx = i_p(t) - N_s \cdot i_s(t) \qquad 4\text{-}1$$

Where H is the magnetic field and α is the angle between the direction of the field and the direction of the small coil element with length dx as shown in Figure 4-1(b).

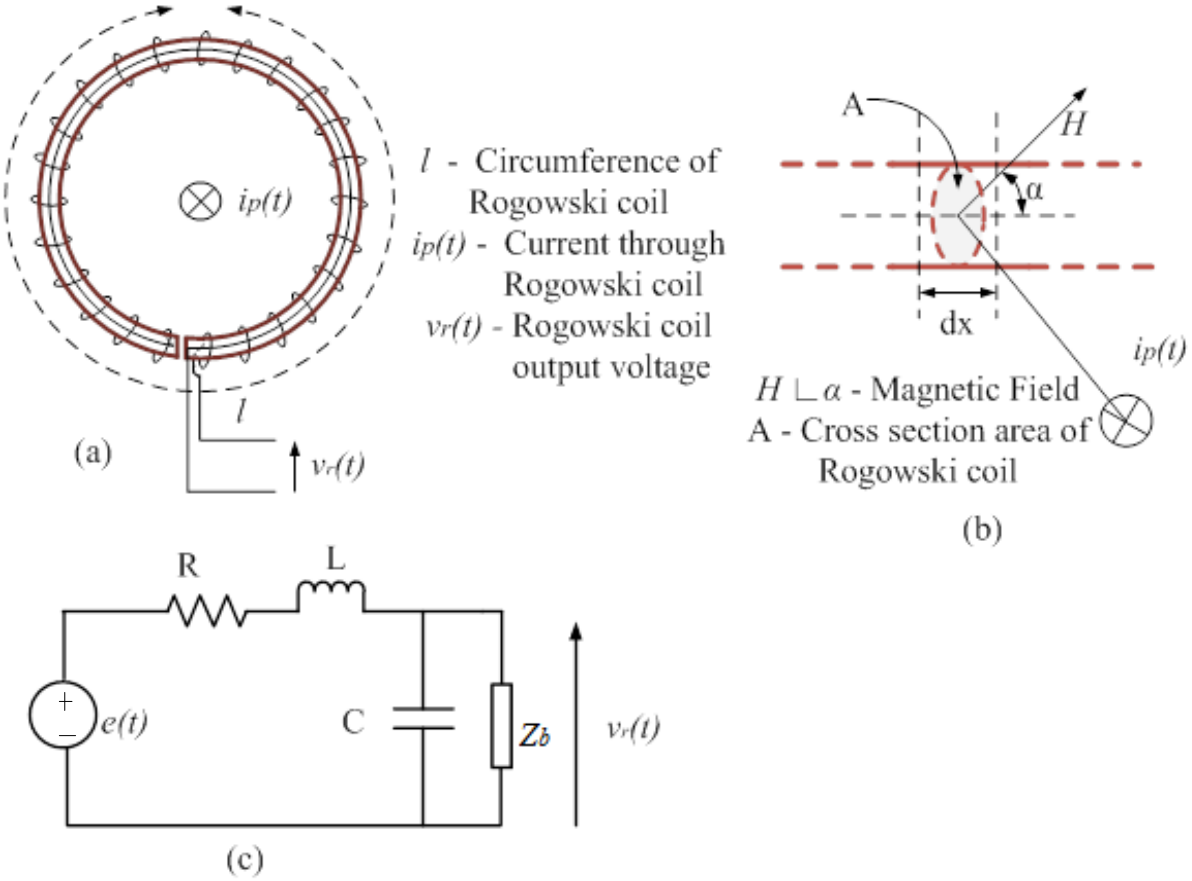

Figure 4-1 (a) Rogowski coil, (b) Expanded view of a small section showing details and (c) Equivalent circuit

The magnetic flux linkage of the elemental coil section is:

$$d\varphi = A \cdot \frac{N_s}{l} dx \cdot \mu_0 \cdot H(t) \cdot \cos(\alpha) \qquad 4\text{-}2$$

The magnetic flux linking the entire coil can be obtained by integrating $d\varphi$ along the coil:

$$\varphi(t) = \oint^{l} d\varphi = \mu_0 \cdot A \cdot \frac{N_s}{l} \oint^{l} H(t) \cdot \cos(\alpha).dx = \mu_0 \cdot A \cdot n \cdot i_p(t) \quad \text{4-3}$$

where $n = N_s/l$ is the number of turns per unit length along the coil or turn density. In (4-3), it is also assumed that $i_s(t)$ is negligible. For accurate measurements, a constant turn density and a constant cross section area along the coil is essential. Any deviation of these parameters will cause deviations in the measurements from the theoretical values. The induced emf on the coil can obtained from Faraday's law as:

$$e(t) = -\frac{d\varphi(t)}{dt} = -\mu_0 \cdot A \cdot \frac{N_s}{l} \cdot \frac{di_p(t)}{dt} \quad \text{4-4}$$

If the quantity to be measured is the primary current, then the output of the Rogowski should be integrated with respect to time. When an integrator is used for calculating the current, it will impose bandwidth limitations and magnitude limits due to integrator slew rate and saturation. However, the application considered in this thesis does not require this integration stage, thus the limitations imposed by the integrator are not a concern. But when the output of the coil is connected to measurement device, a finite secondary current, $i_s(t)$, will flow through the coil. Although this current is very small, at high frequencies, the effects of the coil's self-inductance and parasitic capacitance cannot be ignored. Thus at high frequencies, the Rogowski coil need to be represented by an equivalent circuit consisting of L,R,C and the coil burden Z_b as shown in the Figure 4-1(c) [36]. Application of Kirchhoff's laws to the equivalent circuit in Figure 4-1(c) gives:

$$v_r(t) = e(t) - L \cdot \frac{di(t)}{dt} - i(t) \cdot R \quad \text{4-5}$$

$$i(t) = C \cdot \frac{dv_r(t)}{dt} + \frac{v_r(t)}{Z_b} \quad \text{4-6}$$

By solving (4-5) and (4-6), with $e(t)$obtained from (4-4), the output voltage of the Rogowski coil,$v_r(t)$can be determined.Since the model is to be implemented in an electro-magnetic transient program, solution of (4-5) and (4-6) can be achieved by representing them in state-space format as described below.

$$X(t) = [\, i(t) v_r(t)]^T \qquad 4\text{-}7$$

$$A = \begin{bmatrix} \frac{-R}{L} & \frac{-1}{C} \\ \frac{1}{C} & \frac{1}{Z_b \cdot C} \end{bmatrix} \qquad 4\text{-}8$$

$$U(t) = e(t) \qquad 4\text{-}9$$

$$\dot{X}(t) = A.X(t) + B.U(t) \qquad 4\text{-}10$$

In emt programs, simulation is proceeded in constant time steps. Considering the changes of state variables and input during a single time stepΔt, (4-10) can be written in the form of,

$$\frac{X(t+\Delta t) - X(t)}{\Delta t} = A \cdot \left(\frac{X(t+\Delta t) - X(t)}{2}\right) + B \cdot \left(\frac{U(t+\Delta t) - U(t)}{2}\right) \qquad 4\text{-}11$$

Rearranging (4-11) gives:

$$\left(I - \frac{A.\Delta t}{2}\right).X(t+\Delta t) = \left(I + \frac{A.\Delta t}{2}\right) \cdot X(t) + B \cdot \left(\frac{U(t+\Delta t) - U(t)}{2}\right) \qquad 4\text{-}12$$

$$X(t+\Delta t) = \left(I - \frac{A.\Delta t}{2}\right)^{-1} \cdot \left(I + \frac{A.\Delta t}{2}\right) \cdot X(t) + \left(I - \frac{A.\Delta t}{2}\right)^{-1} .B \left(\frac{U(t+\Delta t) - U(t)}{2}\right) \qquad 4\text{-}13$$

Rogowski coil voltage and the current in the current time step is calculated from the previous time step values of the state variables $i(t)$and , $v_r(t)$.

4.3 Verification of the Rogowski coil model

For verifying the model described above, a Rogowski coil was constructed in the lab. The constructed coil has the parameters given in Table 4-1. Parameters of the Rogowski coil prototype can also be calculated using (4-14) and (4-15)[36][37]. Correctness of the theatrical values obtained using the equations were verified through measurements. A test setup was assembled as shown in Figure 4-2. The primary current was injected using a current amplifier. The Rogowski coil output voltage and the primary current were recorded using a storage oscilloscope. The primary current was measured using a Hall effect sensor having bandwidth of 20 MHz. In order to verify the simulation model, the recorded current measurement obtained from the Hall effect sensor was given as the input to the Rogowski coil model. Then the output of the simulation model and the actual Rogowski coil voltage measured using the oscilloscope were compared.

Table 4-1 Parameters of the Rogowski coil Prototype

Inner radius (b)	51.37 mm	
Outer radius (a)	57.49 mm	
Number of Turns (N_s)	870	
	measured	calculated
Resistance (R)	4 Ω	3.9 Ω
Self-Inductance (L)	81 µH	81 µH
Capacitance (C) *	-	13 pF
Mutual-Inductance (M)	0.093 µH	0.093 µH

* Capacitance is too small to measure

$$L = \frac{\mu_0 . N_s^2}{2.\pi} \cdot (a - b) \cdot \log(b/a) \qquad 4\text{-}14$$

$$C = \frac{2.\pi^2 \cdot \varepsilon_0 \cdot (a + b)}{\log(\frac{b+a}{b-a})} \qquad 4\text{-}15$$

where μ_0 and ε_0 are the relative permeability and relative permittivity of core of the Rogowski coil. N_s is the number of turns and 'a' and 'b' are the inner and outer radii of the coil.

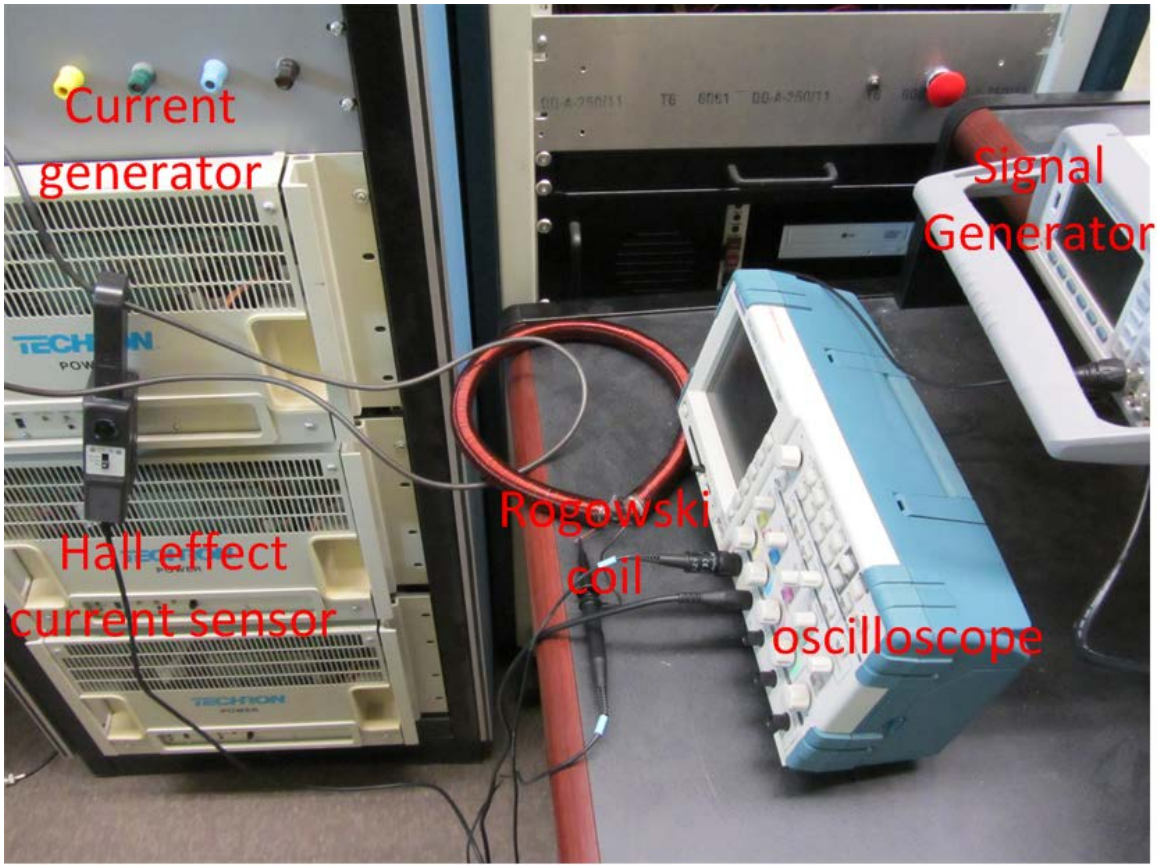

Figure 4-2 Rogowski coil test setup

Figure 4-3 shows an example of the injected primary current during the tests and Figure 4-4 compares the simulation model output and the actual Rogowski coil output for the primary current shown in Figure 4-3. Results of another test are shown in Figure 4-6. These results show

that the Rogowski coil model implemented in PSCAD/EMTDC is accurate. Even though a sharp spike is visible in the experimental Rogowski coil output around 0.13 ms in Figure 4-4, there is no corresponding sharp change visible in the input signal shown in Figure 4-3 during that period. This may be due to lack of bandwidth in the Hall Effect current sensor used to measure the primary current. Since these sharp changes are not present in the input to the model, simulated Rogowski coil outputs do not show those sharp spikes seen in the measured signals.

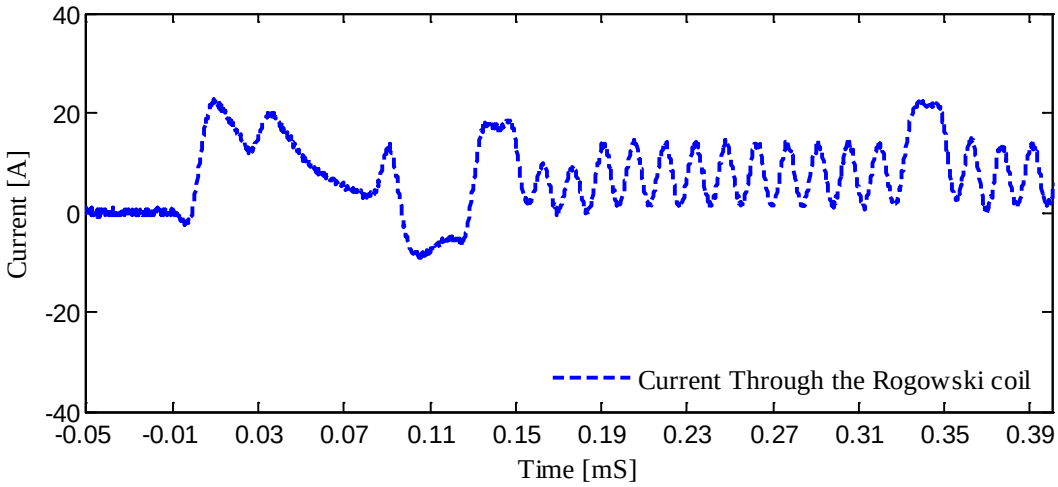

Figure 4-3 Injected primary current to the Rogowski coil

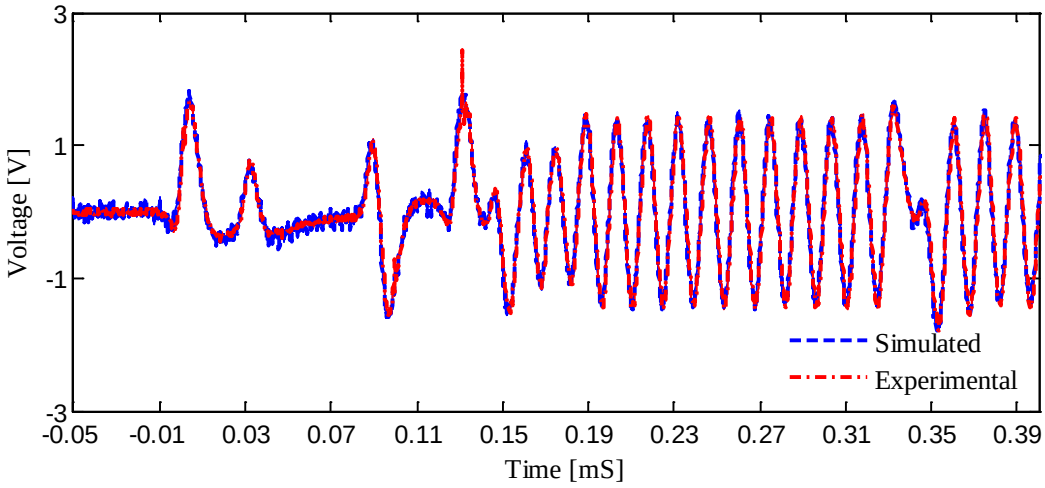

Figure 4-4 Simulated and actual Rogowski coil output voltages

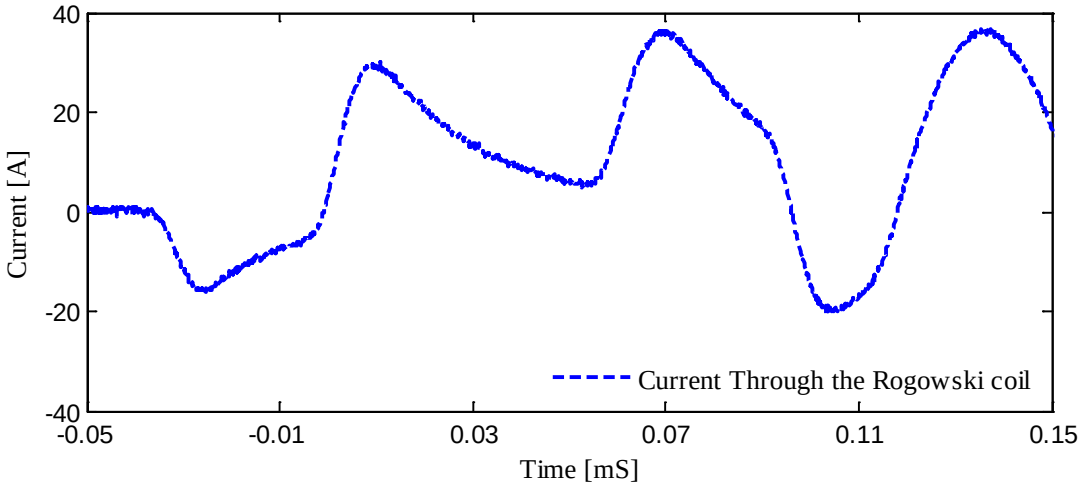

Figure 4-5 Primary current injected to the Rogowski coil

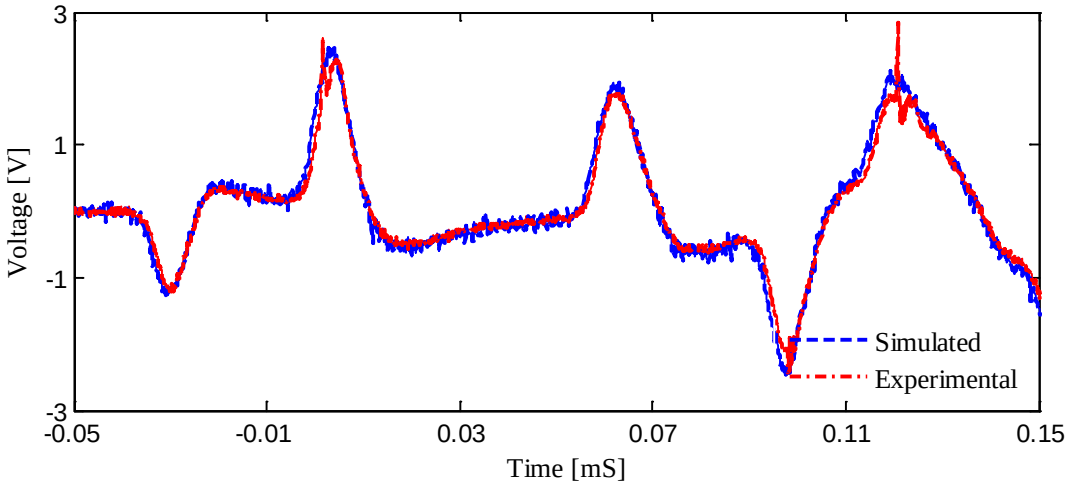

Figure 4-6 Simulated and actual Rogowski coil output voltages

4.4 Concluding remarks

A simulation model of a Rogowski coil was implemented in an EMT program, and the simulation model was verified through experimental tests. This verified simulation model will be used in Chapter 5 for simulating the VSC HVDC line fault location scheme.

Chapter 5

Line Fault Location Performance

5.1 Introduction

Double ended travelling wave based fault location calculation results for a VSC HVDC scheme simulated in PSCAD/EMTDC is presented in this chapter. Two test systems are used in the study. The AC system and the converters used in both test systems are the same. However, the transmission media are different in the two test systems. The first test system consists of a 300 km long cable and the second test system consists of a 1000 km long overhead line. The main objective of this chapter is to present calculated fault locations for two VSC HVDC schemes using the proposed method of detection of travelling waves and analyze the errors caused by different factors.

5.2 Simulated system

The test system used for the simulation study is the same 400 kV (pole-pole) VSC HVDC system described in Chapter-3, and for convenience it is shown again in Figure 5-1. Parameters of the

cable used are shown in Figure 5-2. Rogowski coils were placed around the ground wires of the surge capacitors connected to all four cable terminations. The parameters of the Rogowski coils used are given in Table 5-1. The values of the surge capacitors and series inductors are 100 µF and 10 mH respectively. Data acquisition (DAQ) of the fault location system is assumed to have a sampling frequency of 2 MHz. Thus the simulations were performed at a time step of 0.5 µs.

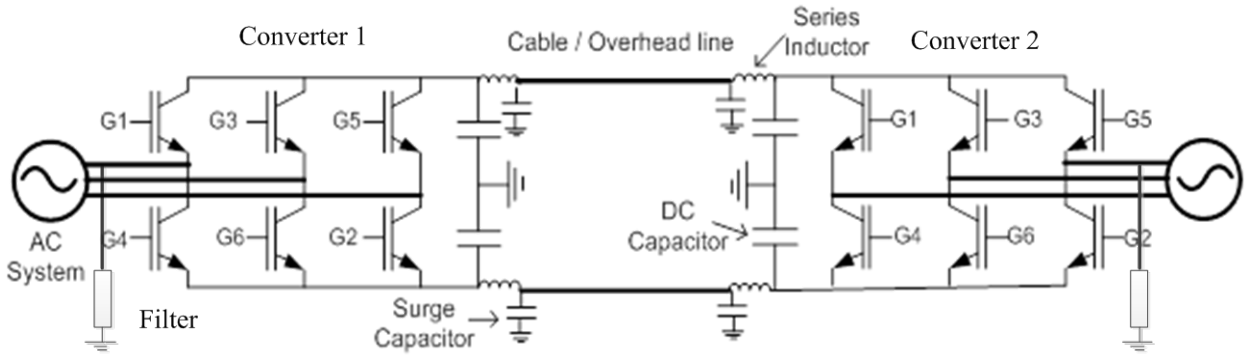

Figure 5-1 400 kV VSC HVDC system

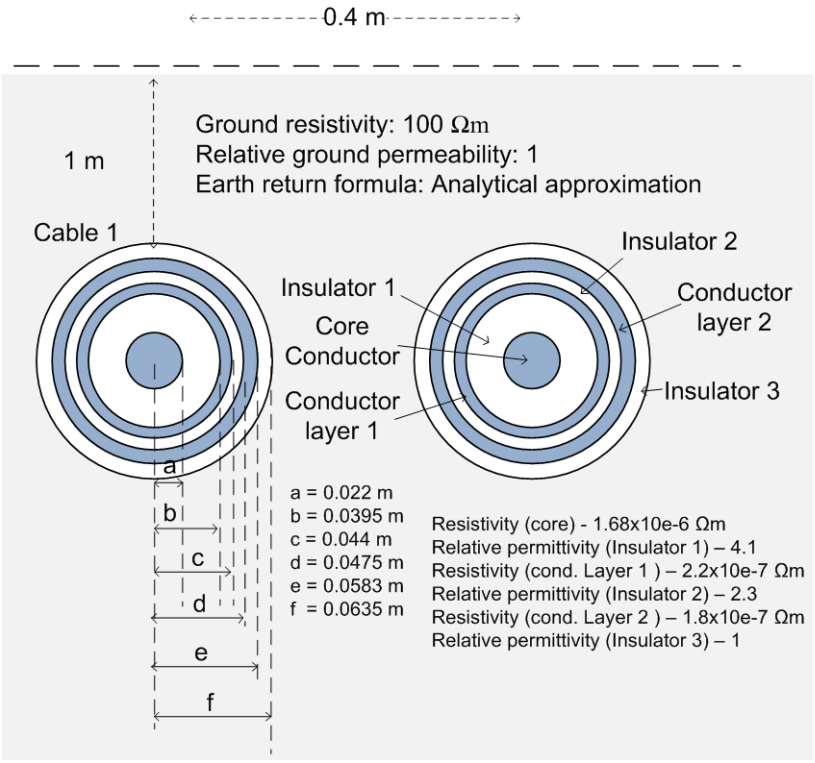

Figure 5-2 Parameters of the Cable

Table 5-1 – Rogowski coil parameters

Inner radius	260 mm
Outer radius	284 mm
Resistance	468 Ω
Self-Inductance	3.5 mH
Capacitance	60.93 pF
Mutual-Inductance	0.55 µH

In order to demonstrate the nature of waveforms, a solid pole-to-ground (P-G) fault was applied on the positive pole, 130 km away from Converter-1. The observed voltages and currents are shown in Figure 5-3. The fault was applied at 0.6 s. On the voltage waveforms, the arrivals of the fault generated wave fronts are clearly observable. Arrivals of some reflected waves are also noticeable on the waveforms. However in double ended method only the time of arrival of the first surge on each end is important. According to the results, the sharp spikes in the output voltages of the Rogowski coil placed on the positive pole indicate accurate measurement of fault generated wave arrival times. Results also show that for a P-G fault on the positive pole, the variations observed on the Rogowski coils placed on the negative pole is insignificant.

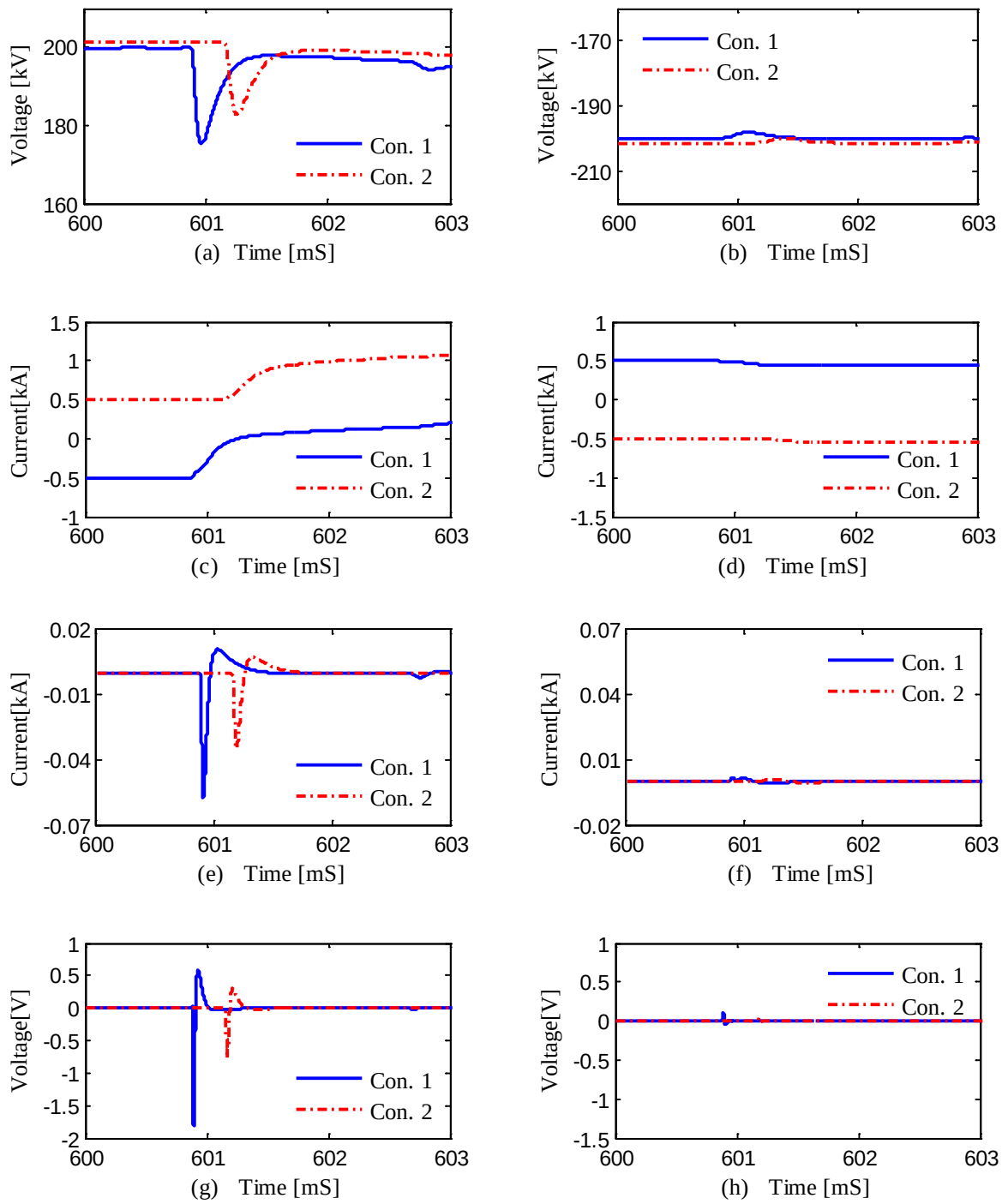

Figure 5-3 Variations of the terminal voltages (a) Positive poles (b) Negative poles, the terminal currents (c) Positive poles (d) Negative poles, the surge capacitor currents (e) Positive pole (f) Negative pole and the Rogowski coil voltages (g) Positive pole (h) Negative pole for solid pole-to-ground fault on positive pole 130 km from Converter-1.

5.3 Fault location calculation

The fault location can be calculated using the double ended method as:

$$X_F = \frac{l - u.(t_{C2} - t_{C1})}{2} \quad \text{5-1}$$

where $(t_{C2} - t_{C1})$ is the difference between the travelling waves arrival times at the two ends, l is the total line/cable length, and u is the velocity of propagation of the travelling wave. The velocity of propagation of the travelling wave can be calculated using cable/line parameters, or it can also be estimated using a test fault at a known location using (5.1).

For this cable based system, the propagation velocity was estimated as 1.46984×10^5 km/s considering a test fault simulated at 5 km from Converter-1. For the fault simulated in Section 5.2, observed arrival times of the travelling waves are: t_{C1}= 600.8765 ms and t_{C2}= 601.1565 ms. Above travelling wave arrival times were determined by visually observing the waveforms. Then the fault location can be calculated as:

$$X_F = \frac{l - u.(t_{C2} - t_{C1})}{2} = 129.422\ km$$

In this case, the fault location was estimated as 129.422 km, instead of actual fault location which is 130 km. This corresponds to an error of -0.578 km. The percentage error of fault location can be calculated as:

$$Error\ = \frac{|Actual\ fault\ location - Calculated\ fault\ location|}{Cable\ length} * 100\% \quad \text{5-2}$$

$$Error = \frac{|129.422 - 130|}{300} \times 100\% = 0.19\%$$

The accuracy of fault location greatly depends on the accurate determination of surge arrival times. Having a sharp change in the signal that used to determine the surge arrival time greatly

increases the accuracy of the fault location scheme. The use of Rogowski coils facilitates accurate detection of travelling waves, since the self-inductance of Rogowski coil is very low compared to the conventional current transformers.

5.4 Threshold setting

Although travelling wave arrival times can be determined through visual inspection of the waveforms, in an automated fault location system, this is generally achieved by comparing the detection waveform against a suitable threshold value. Setting of this threshold affects the determined travelling wave arrival time and hence impacts on the accuracy of the calculated fault location. The threshold should be set sufficiently above the background noise level observed in the detected signal. In practical implementation of the fault locator, the threshold values should be set during the commissioning after observing the actual noise levels. The field test results presented in Chapter-3 indicate that the noise levels observed on the Rogowski coil output voltage is quite low (± 4 mV), and therefore, these thresholds can be very small compared to the observed peak voltages. In this section, the impact of the threshold on fault location accuracy is examined. It should also be noted that the thresholds affect the estimation of propagation velocity as well, if the velocity is estimated using a test fault.

When a fault occurs close to one of the terminal, the travelling wave arriving at the closer terminal travels a shorter distance and hence subjected to less attenuation. Thus the measurements at the close by terminal would show very large and sharp change in the detection signal (in this case the voltage of the Rogowski coil placed on the surge capacitor grounding circuit). On the other hand, the wave travelling towards the remote end travels a longer distance

and subjected to attenuation along the distance it travels. Consequently, the sharpness of the wave front is reduced when it finally arrives at the terminal. Thus the measurements at the remote terminal would show a smaller surge with less sharp wave front. But since the travelling wave arrival time is obtained by comparing the signal against the same threshold value, an error can be introduced to the measured surge arrival time difference.

The threshold selection criteria used throughout the thesis is as shown in Figure 5-4. If the peak-to-peak signal variation (due to noise from the converters and other sources) during the pre-fault period is *Vn*, then the Threshold X is set (*Vn·X*) above the maximum no fault signal level. A negative threshold is set (*Vn·X*) below the minimum pre-fault signal level. For example, 'Threshold 10' is set 10 times the peak-to-peak noise level above the steady state signal level.

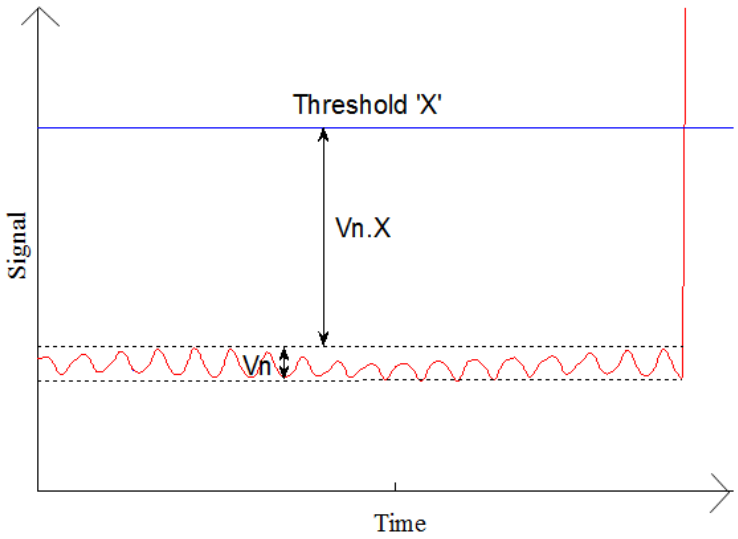

Figure 5-4 Threshold selection criteria

Figure 5-5 illustrates how the thresholds level is affecting the estimated time difference, when the signals observed at the two ends have different slopes. Depending on the thresholds selected accuracies of the fault location calculation may change.

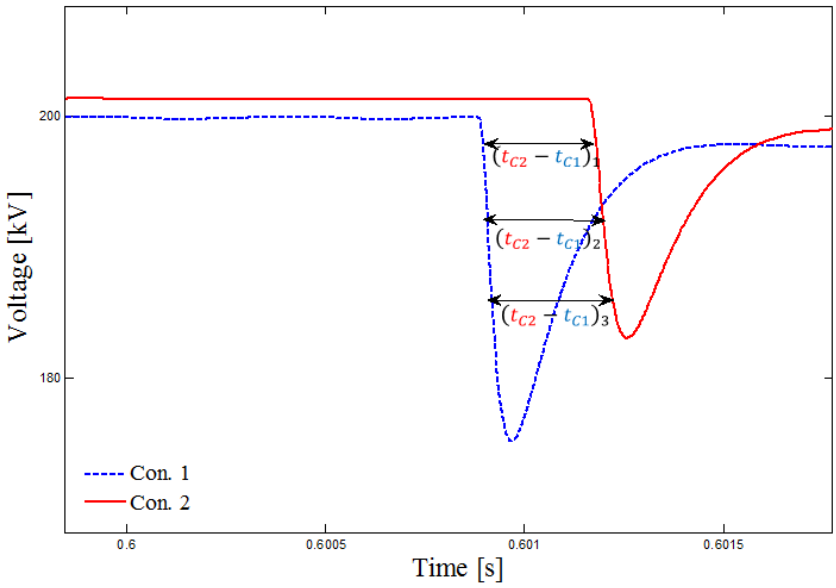

Figure 5-5 Threshold settings

A solid P-G fault was applied 130 km from Converter-1 on the positive pole. The voltages observed at the output of Rogowski coils on the positive pole of the two ends are shown in Figure 5-6 and Figure 5-7. To compare the accuracy of fault location based on visual inspection and threshold settings, the following example calculation is presented. The thresholds were set as explained earlier considering the signal noise levels. For example, if the steady state signal varies in the range of -1 mV to +2 mV, then with a 3 mV margin (that is 100% of the peak-to-peak noise), the upper threshold is set at +5 mV and the lower threshold is set at -4 mV.

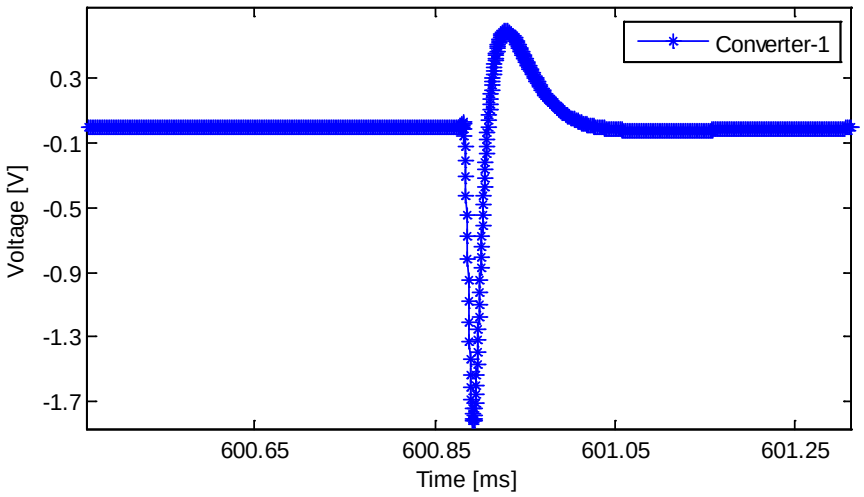

Figure 5-6 Converter 1 side Rogowski coil voltage for a solid fault 130 km from Converter-1.

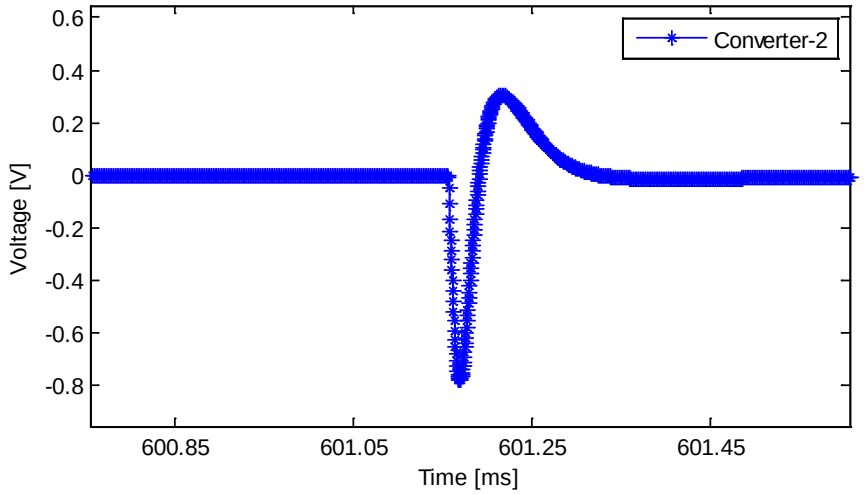

Figure 5-7 Converter-2 side Rogowski coil voltage for a solid fault 130 km from Converter-1.

For the fault example shown in Figure 5-6 and Figure 5-7, the travelling wave arrival times at the two ends are estimated by visual inspection as:

$t_{C1} = 600.8765\ ms$

$t_{C2} = 601.1565\ ms$

The velocity of propagation of the fault generated travelling waves was estimated from a test fault simulated at 5 km from the rectifier end, again the travelling wave arrival times determined

by visual Inspection. The estimated propagation velocity was 1.46984×10^5 km/s. The length of the cable is 300 km. Thus the estimated fault location is

$$X_F = \frac{l - u.(t_{C2} - t_{C1})}{2} = 129.422\ km$$

For the same fault, the travelling wave arrival time obtained using a threshold setting with a margin of 10 times the peak-to-peak noise, (referred to as "Threshold-10") are:

$t_{C2} = 600.8780\ ms$

$t_{C1} = 601.1575\ ms$

The velocity of propagation estimated from the same test fault as above (5 km from the rectifier end) with Threshold-10 is 1.46454×10^5 km/s. The calculated fault location is,

$$X_F = \frac{l - u.(t_{C2} - t_{C1})}{2} = 129.547\ km$$

For this particular fault, the fault distance estimated with threshold setting "Theshold-10" seems to be more accurate than the value obtained with the visual inspection. The fault location errors are compared for a number of faults at different locations with three different threshold settings: Threshold-1 corresponds to a margin of 100% of the peak-to-peak pre-fault signal, Threshold-10 corresponds to a margin of 1000% of the peak-to-peak pre-fault signal and Threshold 25 corresponds to a margin of 2500% of the peak-to-peak pre-fault signal. The results are presented in Table 5-2.

Table 5-2 Comparison of fault location errors for different threshold settings and for visual inspection method

Actual fault location (*km*)	Fault location errors (*km*)			
	visual inspection	Threshold 1	Threshold 10	Threshold 25
30	0.233	0.209	-0.209	0.097
50	0.721	0.707	0.326	0.123
130	0.578	0.567	0.453	0.193
160	-0.476	-0.394	-0.172	-0.115
230	-0.327	-0.286	-0.019	0.106
260	-0.863	-0.807	-0.424	-0.165

According to the results given in Table 5-2, the fault location errors for the visual inspection method are similar to those achieved with a smaller threshold such as 'Threshold-1'. This is expected, as visual inspection is equivalent to using the smallest possible threshold. The results in Table 5-2, show that the fault locations obtained with the two large thresholds (Threshold-10 and Theshold-25) are more accurate than those obtained with the visual inspection method and with the low threshold. This is an observation which is contrary to the expectation.

In order to better understand how the threshold is impacting on the accuracy, further simulations were carried out with a wide range of threshold settings. Furthermore, the fault resistance was also varied during these simulations. The simulation results indicate that the accuracy of the fault location depends on the fault resistance as well as on the threshold values selected. Each graph shown in Figure 5-8 to Figure 5-12 shows the variations of the fault location errors with the threshold setting for particular fault location. The three curves in the each graph are obtained

with three different fault resistances (0Ω, 50Ω, and 100Ω). The x-axis of the graphs is threshold in terms of the size of margin as a multiple of the peak-to-peak signal during the normal operation.

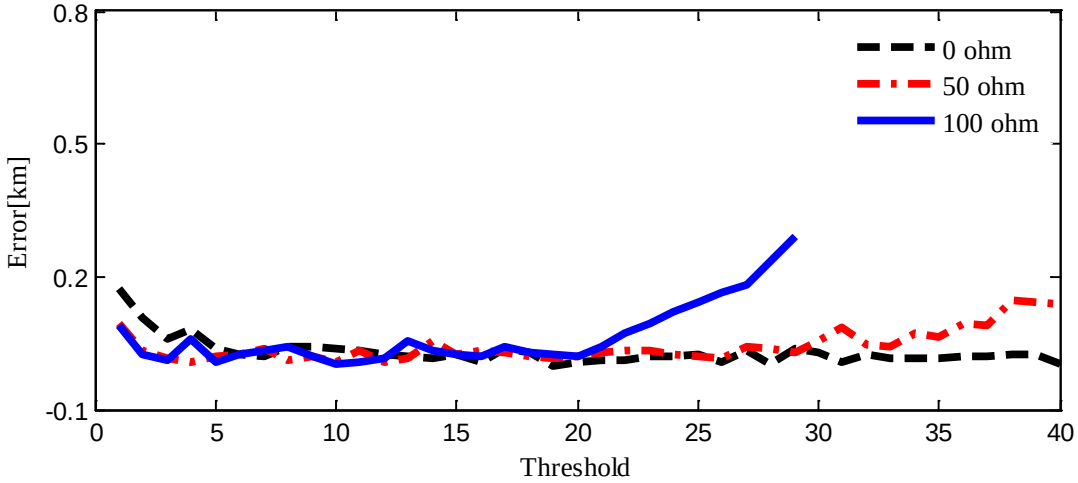

Figure 5-8 Variation of the fault location error with the threshold level for a fault 30km the Converter -1

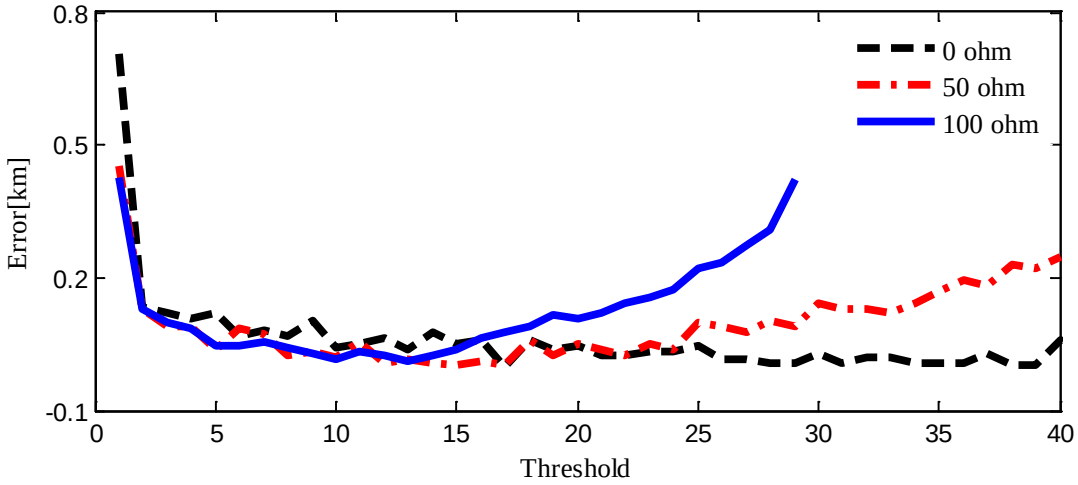

Figure 5-9 Variation of the fault location error with the threshold level for a fault 50km the Converter -1

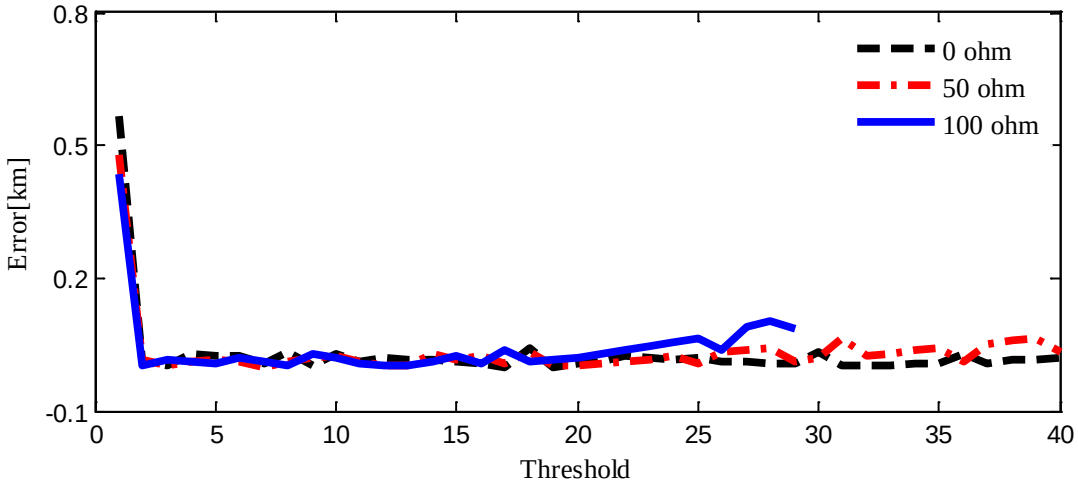

Figure 5-10 Variation of the fault location error with the threshold level for a fault 130km the Converter -1

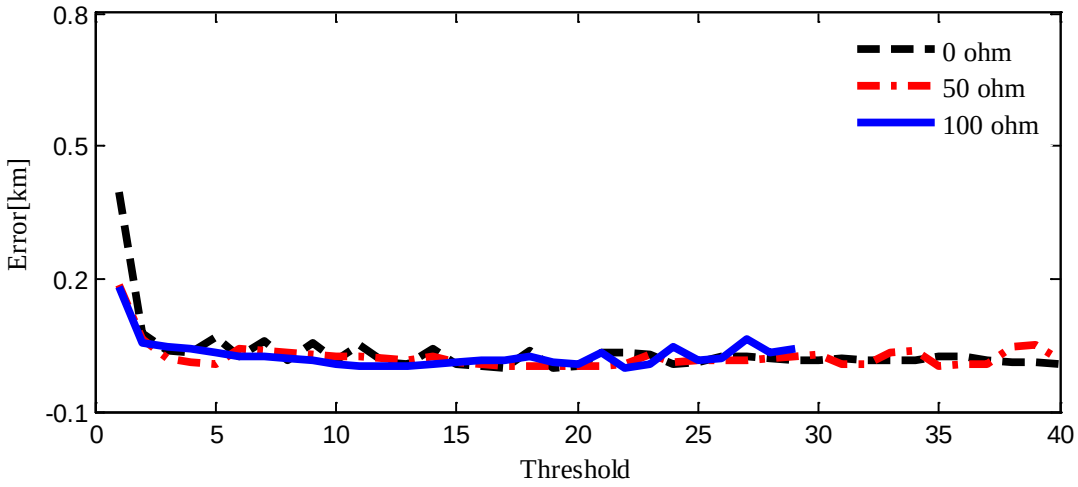

Figure 5-11 Variation of the fault location error with the threshold level for a fault 160km the Converter -1

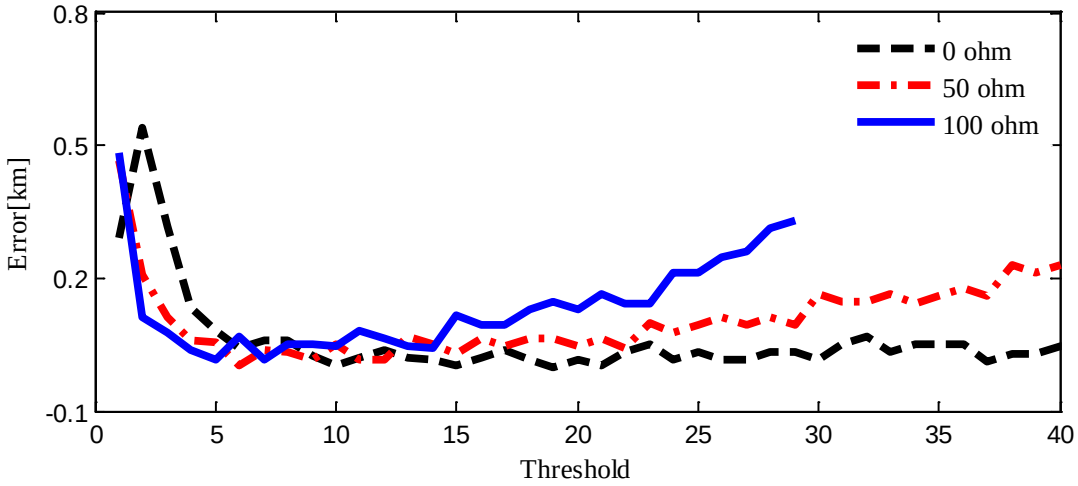

Figure 5-12 Variation of the fault location error with the threshold level for a fault 220 km the Converter -1

The general trend observed from these graphs is that when the threshold is very small, error is larger. When the threshold is increased, the error is reduced but further increase of threshold increasing the error again. This suggests that there is some optimum threshold setting. After this optimum threshold, the errors start to rise with the increasing threshold. When the fault resistance is high, this drop in accuracy is faster. At very high fault resistances, the wave fronts become undetectable with larger thresholds. It is also evident that the influence of the threshold is not very significant when the fault is close the middle of the cable. This is expected because when the fault is in the middle; both travelling waves will travel approximately the same distance, subjecting to similar level of attenuation. When consider only the solid faults, the optimum threshold setting falls around 20 times the peak-to-peak noise level. However when a range of fault resistances are considered, the optimum threshold is around 10 times the pre-fault peak-to-peak signal. If this optimum threshold value is selected, the maximum fault location error will not be significantly affected by the fault resistance.

Main conclusions that can be arrived at from the above simulation experiments are that the accuracy of the fault location calculation change with the threshold values used. Therefore, selecting a threshold should be done carefully after observing the pre-fault signal and noise levels. The simulations results suggest that use of the lowest possible threshold is not the optimum. A possible approach for determining the proper thresholds for a practical HVDC line fault location system is to apply a test fault during the commissioning to (i) determine the propagation velocity, (ii) estimate the background noise in signals, and (iii) calibrate a simulation model. Then a simulation study similar to the one described above can be performed using the calibrated model with an added noise to the detection signals (at a level similar to the noise observed during the commissioning tests) to determine the optimum thresholds. Further examination of the accuracy of the fault location calculation at very low threshold levels and visual inspection shows that accuracy slightly increases with the increasing fault resistance, at low thresholds. This is evident from the example shown in Figure 5-13.

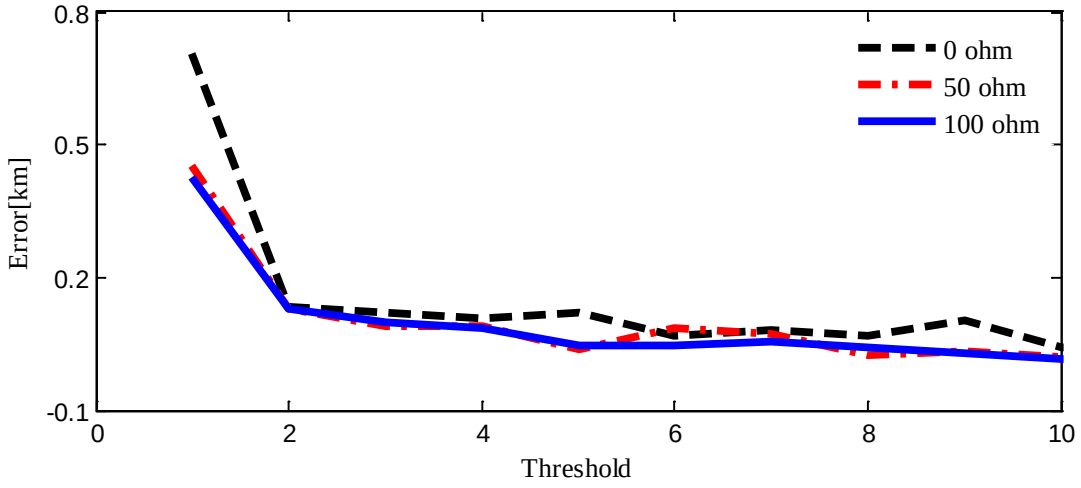

Figure 5-13 Variations of the fault location error with the threshold for a fault 50km from the Converter -1 (for low threshold values)

5.5 Modal transform

The phases of a transmission line are tightly coupled due to mutual impedances and admittances between the phases. One way to accomplish the calculations of currents and voltages in multi-phase lines is to represent them in modal domain, where its *n* coupled phases are represented by their *n* propagation modes, which are uncoupled. The separation line in their modes of propagation is through the use of a modal transformation matrix whose columns are eigenvectors associated with the parameters of the line. A bipolar DC line can be treated as a two phase system, and the voltages are currents can be transformed into areal and ground mode voltages and currents. The two modes have distinct propagation velocities, and therefore it is expected that calculation of fault location using modal signals (voltages or currents) to be more accurate. The direct application of measured voltages (which can be considered as phase voltages) that contain components of both modes to fault location with a single propagation velocity could result in errors. In this section attempt was made to examine if the accuracy can be improved by using modal signal for fault location estimation.

The phase to modal transformation of bipolar dc system is:

$$\begin{bmatrix} u_{m0} \\ u_{m1} \end{bmatrix} = T.\begin{bmatrix} u_N \\ u_P \end{bmatrix} \begin{bmatrix} i_{m0} \\ i_{m1} \end{bmatrix} = T.\begin{bmatrix} i_N \\ i_P \end{bmatrix} \qquad 5\text{-}3$$

Where, T is the phase-modal transformation matrix, u_P and u_N are the DC voltage on positive and negative polar line, i_P and i_N are the DC current on positive and negative polar line, u_{m0} and u_{m1} are defined as “0” and “1” modal circuit voltages,i_{m0} and i_{m1} are defined as “0” and “1” modal circuit currents. The transformation matrix is frequency dependent if the line is not ideally transposed. However, it can be approximated by a constant real transformation matrix with some

small error even for the other cases. In order to guarantee the power of system is equal before and after the transformation, orthogonal transformation matrix in (5-4) is used.

$$T = \frac{1}{\sqrt{2}}\begin{bmatrix}1 & 1\\ 1 & -1\end{bmatrix} \quad 5\text{-}4$$

By substituting 5-3 into 5-4, the modal voltages and currents are obtained as

$$u_{m0} = \frac{1}{\sqrt{2}}u_N + \frac{1}{\sqrt{2}}u_P u_{m1} = \frac{1}{\sqrt{2}}u_N - \frac{1}{\sqrt{2}}u_P \quad 5\text{-}5$$

$$i_{m0} = \frac{1}{\sqrt{2}}i_N + \frac{1}{\sqrt{2}}i_P i_{m1} = \frac{1}{\sqrt{2}}i_N - \frac{1}{\sqrt{2}}i_P \quad 5\text{-}6$$

5.5.1 Modal transformation of the Rogowski coil voltages

It can be shown that the same modal transformation matrix used to transform terminal (phase) voltages into modal components can be used to transform the Rogowski coil voltages into its modal components. In mathematics the linearity of differentiation and scaling are most fundamental properties. Differentiating5-5:

$$\dot{u}_{m0} = \frac{1}{\sqrt{2}}\dot{u}_N + \frac{1}{\sqrt{2}}\dot{u}_P \dot{u}_{m1} = \frac{1}{\sqrt{2}}\dot{u}_N - \frac{1}{\sqrt{2}}\dot{u}_P \quad 5\text{-}7$$

Taking the derivate again:

$$\ddot{u}_{m0} = \frac{1}{\sqrt{2}}\ddot{u}_N + \frac{1}{\sqrt{2}}\ddot{u}_P \ddot{u}_{m1} = \frac{1}{\sqrt{2}}\ddot{u}_N - \frac{1}{\sqrt{2}}\ddot{u}_P \quad 5\text{-}8$$

Scaling is a linear operation:

$$k\ddot{u}_{m0} = \frac{1}{\sqrt{2}}k\ddot{u}_N + \frac{1}{\sqrt{2}}k\ddot{u}_P \ddot{u}_{m1} = \frac{1}{\sqrt{2}}k\ddot{u}_N - \frac{1}{\sqrt{2}}k\ddot{u}_P$$

$$\begin{bmatrix}k\ddot{u}_{m0}\\ k\ddot{u}_{m1}\end{bmatrix} = \frac{1}{\sqrt{2}}\begin{bmatrix}1 & 1\\ 1 & -1\end{bmatrix}.\begin{bmatrix}k\ddot{u}_N\\ k\ddot{u}_P\end{bmatrix} \quad 5\text{-}9$$

Note that Rogowski coil output voltage, v_r is approximately equal to $M\frac{di_s}{dt}$ where M is the mutual inductance of the Rogowski coil and i_s is the current flowing in the primary conductor going through the Rogowski coil [38]. Since the current flowing through the primary conductor is the surge capacitor current, ($i_s = C\frac{du}{dt}$), where u is the terminal voltage, the Rogowski coil output voltage is approximately equal to $MC\frac{du^2}{dt^2}$. The by replacing $k\ddot{u}_N$ and $k\ddot{u}_P$ in (5-9) with the Rogowski coil voltages, the model components of the Rogowski coil voltages can be found,

$$\begin{bmatrix} v_{rm0} \\ v_{rm1} \end{bmatrix} = \frac{1}{\sqrt{2}}\begin{bmatrix} 1 & 1 \\ 1 & -1 \end{bmatrix}\begin{bmatrix} v_{rN} \\ v_{rP} \end{bmatrix} \qquad 5\text{-}10$$

The modal components of the Rogowski coil voltages can then be used to calculate the fault locations. Table 5-3 shows errors for solid P-G faults obtained with this approach in comparison to direct use of Rogowski voltages. Table 5-4 shows the errors for P-G faults with 100Ω fault resistance. Threshold used to detect the travelling wave is 100% of the peak-to-peak pre-fault signal noise.

No significant difference can be seen between the accuracies obtained with the modal transformed Rogowski coil voltages and the direct Rogowski coil output voltages. It can be concluded that taking the modal components of the Rogowski coil voltages does not considerably improve the accuracy of fault location calculation.

Table 5-3 Fault location error comparison with modal transform for solid faults

Actual fault location (km)	Fault location error (km)		
	No Modal Transform	Mode '0'	Mode '1'
30	0.209	0.172	0.209
50	0.707	0.707	0.707
130	0.567	0.567	0.567
160	-0.394	-0.467	-0.431
230	-0.286	-0.286	-0.286
260	-0.807	-0.807	-0.807

Table 5-4 Fault location error comparison with modal transform for faults with 100Ω fault resistance

Actual fault location (km)	Fault location error (km)		
	No Modal Transform	Mode '0'	Mode '1'
30	-0.088	-0.119	-0.095
50	0.427	0.402	0.452
130	0.474	0.432	0.479
160	-0.182	-0.179	-0.404
230	-0.100	-0.080	-0.120
260	-0.499	-0.508	-0.527

5.6 Fault location with filtered signals

Velocities of the different frequencies of the travelling wave being different can be one of the reasons for the errors occurred. According to the observations, after a fault close to Converter-1, the travelling wave arriving at Converter-1 has a wave front with a very sharp rising slope, and hence contains frequency components of higher order. The corresponding travelling wave arriving at Converter-2 is subjected to more attenuation along the line, and the wave front observed at Converter-2 terminal is characterized with a more gradual increase in the voltage. This indicates that the travelling waves arriving at far end (Converter-2) do not contain some of the high frequency components that were present in the travelling wave arriving at Converter-1.

To investigate difference in frequency content of the terminal voltage, a solid P-G fault was applied at 5 km away from the Converter-1.Voltages measured at the two ends are shown in Figure 5-14. Note that before plotting, the mean of the signal was removed from both signals, and the voltage measured at Converter-1terminal (labeled as 5 km) was scaled down to the range of that measured at Converter-2 terminal (labeled as 295 km). The comparison of frequency spectrums of these two signals shown in Figure 5-15 clearly indicates that signal measured at closer end contain more high frequency signal content.

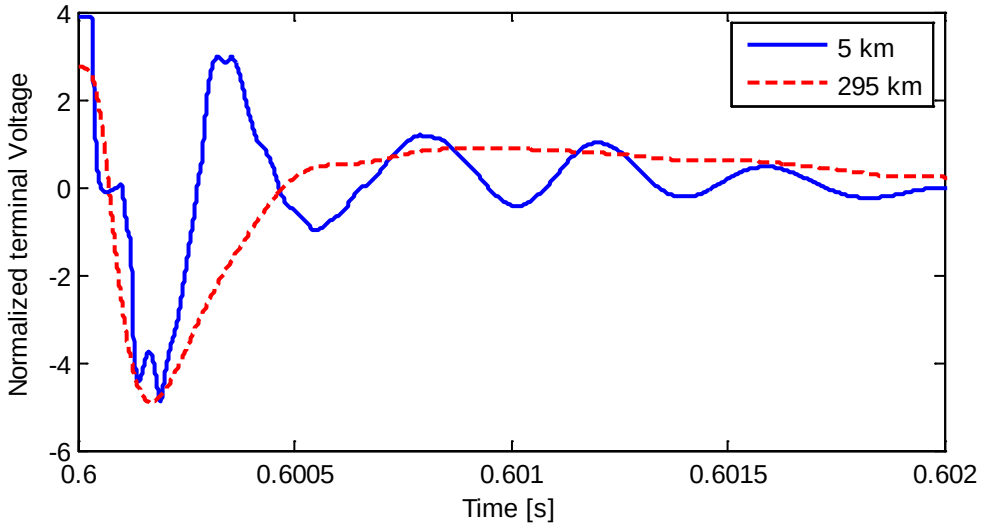

Figure 5-14Terminal voltages

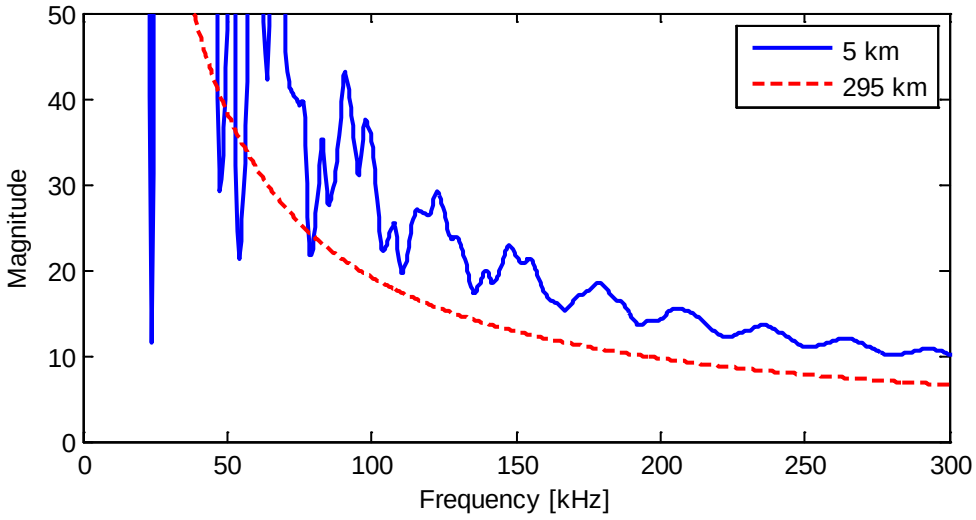

Figure 5-15Frequency spectrum of terminal voltages

Because the signals at different frequencies travel at different velocities [40], using two signals which contain different frequency components may introduce error to the fault location calculation. If both signals are filtered to have similar frequency contents, the accuracy of fault location may be improved. In order to test this hypothesis, the voltage signals were filtered using

a 5^{th} order low pass Butterworth filter. Examples of the filter magnitude and phase characteristics (for cut-off frequency = 100 kHz) are shown in Figure 5-16. A comparison of the filtered signals is shown in Figure 5-17. The frequency spectrums of the filtered signals are compared in Figure 5-18. After the filtering, the frequency spectrums of the signals measured at the two ends are much similar in the shape.

In order to investigate whether filtering can improve the fault location accuracy, the signals used to detect the wave fronts (Rogowski coil voltages) were low pass filtered before comparing with the threshold. Examples of the filtered and unfiltered Rogowski coil voltages are shown in Figure 5-19. The filtering introduce a time shift, but this time shift would not be an issue, as signals measured at both ends are filtered using the same filter. When taking the time difference, the effect of time shift gets cancelled out. Accuracy of fault location was determined for faults at different locations with filtered signals. The experiments were repeated with filters having different cut-off frequencies (1 MHz, 500 kHz, 100 kHz, 50 kHz, and 10 kHz).

The thresholds for the filtered signal were set as described in Section 5.4, but now considering the steady state signal variation in the filtered signal. For example, Threshold-10 now means a threshold set with a margin of 10 times the peak-to-peak noise observed in the filtered signal. In case of 100 kHz low pass filter steady state signal noise is almost as same as that of the unfiltered signal as can be seen in Figure 5-19(b).The major part of the steady state noise in the signal is due to the switching of IGBTs in the converter and therefore of has a frequency much lower than the cut-off frequency of the filter, 100 kHz. However, in the case of filters with lower cut-off frequencies, the steady state noise gets somewhat attenuated.

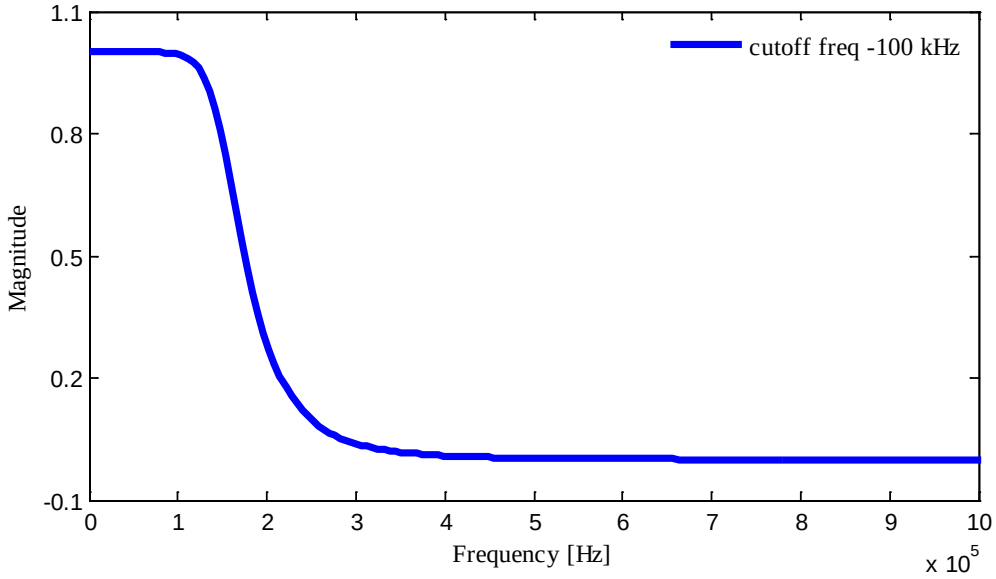

(a)

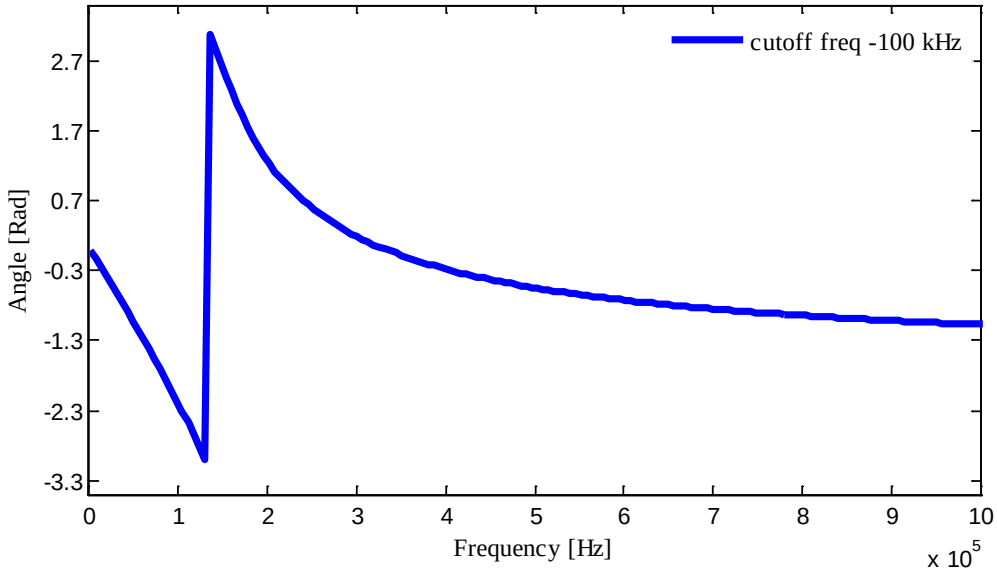

(b)

Figure 5-16 Characteristics of the 5th order low pass Butterworth filter with a cut-off frequency of 100 kHz

(a) Magnitude (b) Phase

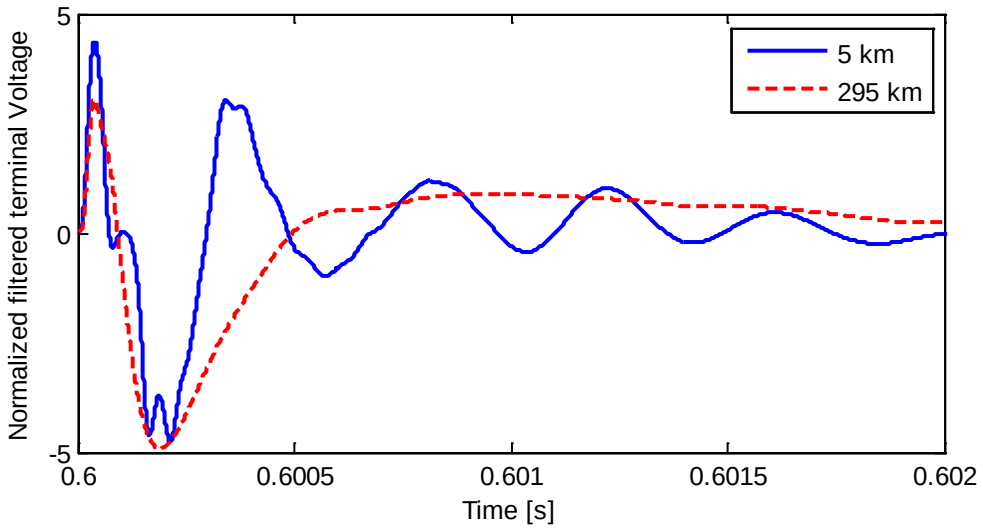

Figure 5-17Filtered terminal voltages

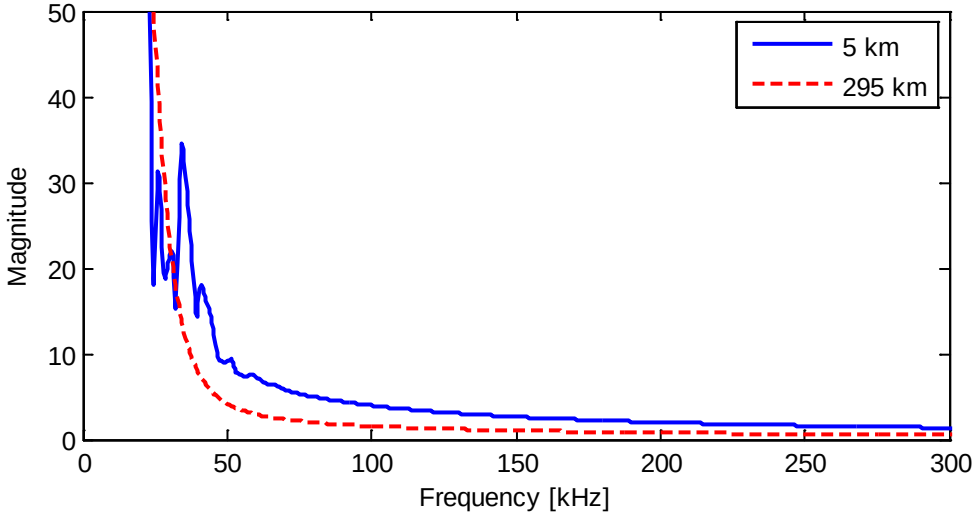

Figure 5-18Frequency spectrum filtered terminal voltages

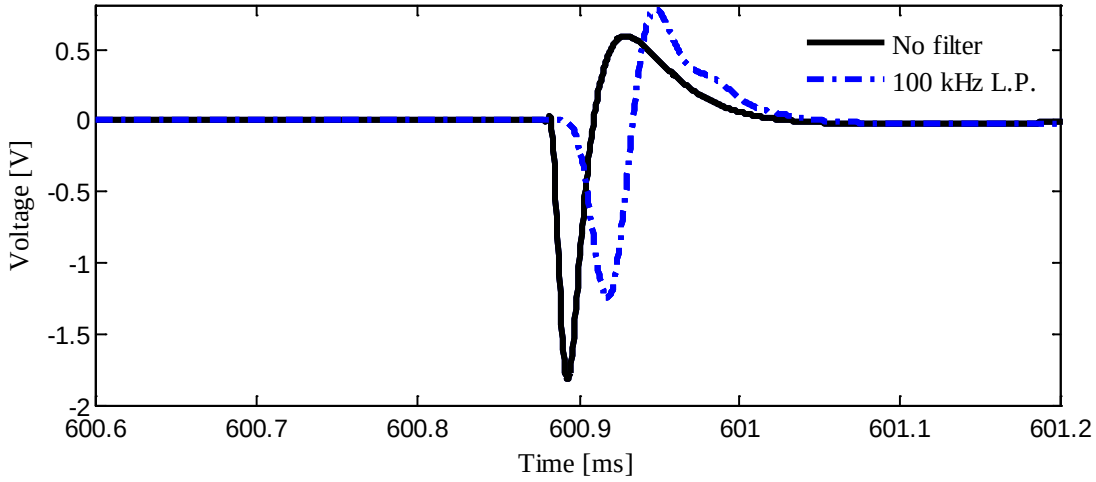

(a)

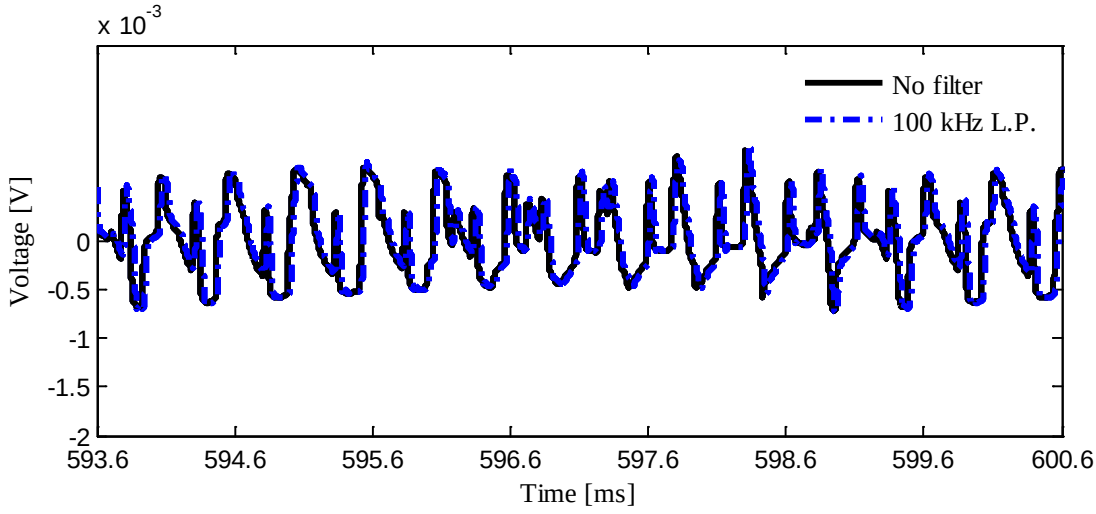

(b)

Figure 5-19 (a) filtered and unfiltered Rogowski coil voltages for a solid P-G fault 130 km away from the Converter-1. (b) Zoomed y-axis during steady state.

Solid pole-to-ground faults were simulated at six different locations. Fault location errors for different filter cut-off frequencies are shown in Table 5-5. Threshold setting used for these calculations is 'Threshold-1' (a very low threshold). Results shown in Table 5-5 show that filtering improves the accuracy substantially. Initially the fault location accuracy improves when

lowering the filter cut-off frequency. However, if the filter cut-off frequency is reduced below 50 kHz, the accuracy starts to decrease again. The best accuracies are obtained for the cut-off frequencies 100 kHz and 50 kHz.

Table 5-5 Fault location errors with filtered detection signals (Threshold-1 / Solid fault).

Actual fault location (km)	Fault location error (km)					
	No filter	1MHz	500 kHz	100kHz	50kHz	10kHz
30	0.172	0.161	0.112	-0.095	0.071	0.159
50	0.707	0.641	0.576	0.163	0.114	-1.63
130	0.567	0.510	0.452	-0.004	0.030	-1.121
160	-0.394	-0.31	-0.190	-0.089	-0.015	1.164
230	-0.286	-0.278	-0.197	-0.203	-0.011	52.462
260	-0.807	-0.731	-0.619	-0.216	-0.129	67.948

In order to investigate the effect of fault resistance, the same experiment was repeated with a fault resistance of 100Ω. Results are shown in Table 5-6. Even for high resistance faults, the signals filtered with a low pass filter having a cut-off frequency of 100 kHz and 50 kHz gives the most accurate results.

In order to examine the sensitivity of fault location accuracy to threshold setting, the above two experiments were repeated again with Threshold-10 (a threshold with a larger margin). The fault location errors for the cases of solid faults and faults with 100 Ω fault resistance are shown in Table 5-7 and Table 5-8. According to the results, again filtered signals give better accuracy, with 100 kHz and 50 kHz cut-off frequencies producing the lowest errors.

Table 5-6Fault location errors with filtered detection signals (Threshold-1/ Fault resistance 100Ω).

Actual fault location (km)	Fault location error (km)					
	No filter	1MHz	500 kHz	100kHz	50kHz	10kHz
30	-0.088	-0.136	-0.117	0.058	0.140	0.804
50	0.427	0.362	0.359	0.206	0.129	-2.195
130	0.474	0.380	0.182	-0.003	0.011	-1.510
160	-0.182	-0.172	-0.164	-0.071	0.012	1.723
230	-0.100	-0.056	-0.068	-0.135	0.064	53.374
260	-0.499	-0.424	-0.414	-0.204	-0.152	68.969

Table 5-7 Fault location errors with filtered detection signals(Threshold-10 / Solid fault).

Actual fault location(km)	Fault location error (km)					
	No filter	1MHz	500 kHz	100kHz	50kHz	10kHz
30	-0.209	-0.221	-0.165	-0.038	0.040	0.373
50	0.326	0.297	0.258	0.041	0.057	-0.057
130	0.453	0.176	0.015	0.030	0.019	-0.305
160	-0.172	-0.125	-0.117	-0.015	0.009	0.03
230	-0.019	-0.011	-0.024	-0.048	0.034	-0.039
260	-0.424	-0.349	-0.302	-0.056	-0.012	-0.333

Table 5-8 Fault location errors with filtered detection signals (Threshold 10 / Fault resistance 100Ω).

Actual fault location(km)	Fault location error (km)					
	No filter	1MHz	500 kHz	100kHz	50kHz	10kHz
30	0.031	-0.016	0.069	-0.004	0.051	2.354
50	-0.016	-0.044	-0.021	0.015	0.012	-7.37
130	0.011	0.028	-0.019	-0.019	0.002	-2.04
160	-0.097	-0.050	-0.045	-0.009	0.035	0.816
230	0.028	0.035	0.003	0.039	0.133	6.053
260	-0.008	0.030	0.013	0.012	0.094	-2.886

Figure 5-20 shows the variation of the fault location error with the location of the fault for solid faults, when the calculations are done using the signals filtered with a 100 kHz low pass filter. The graph was generated considering a large number of fault locations along the 300 km long cable, and a thresold with a margin of 10 times the noise level. Figure 5-21 show the same when the faults are having a fault resistance of 100Ω. Two graphs show that errors are less than 100 m for all the faults considered. This is an improvement when compared with the accuracy obtained with the unfiltered signals. Also, the results show consistaently higher accuracy for the high impedance faults.

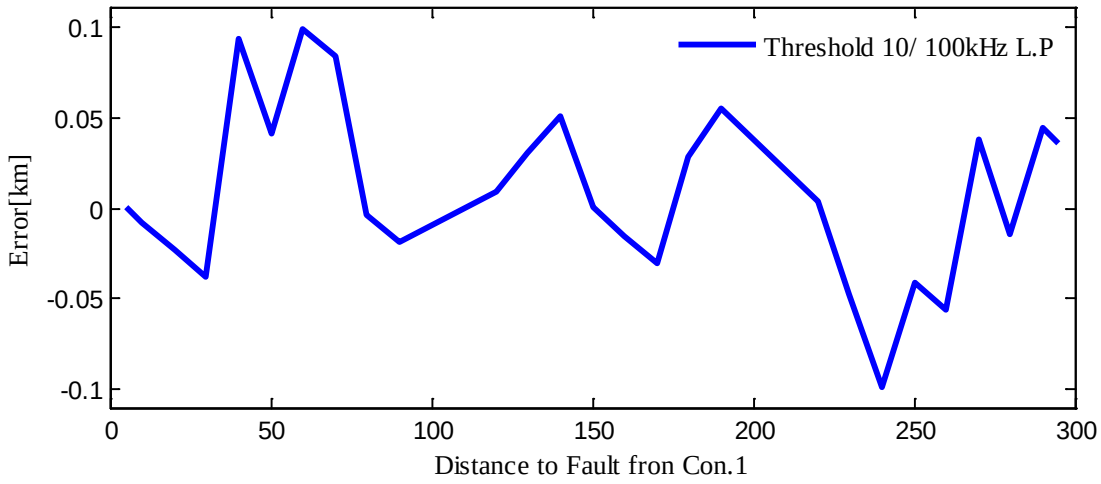

Figure 5-20 Variation of fault location error for solid faults when the detection signal is filtered with a 100 kHz low pass filter

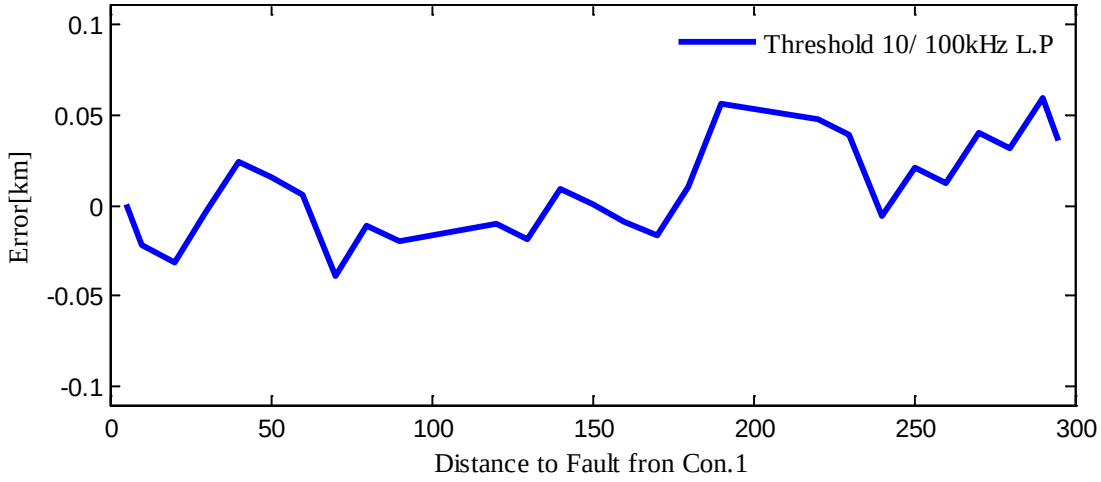

Figure 5-21 Variation of fault location error for high resistance faults (100Ω) when the detection signal is filtered with a 100 kHz low pass filter

From the results of this simulation experiment, it can be concluded that filtering of the detection signal using a low pass filter in the range of 50-100 kHz improves the fault location accuracy, confirming the initial hypothesis. This improvement can be attributed to the fact that the signal

components with different frequencies travel at different velocities [40], and when the signals measured at the both ends is band limited to the same highest frequency through filtering, fault location is most probably estimated considering the signal components at that highest frequency.

Cut-off frequency of the filter used in this test network may not be the optimum cut-off frequency for another network having longer or shorter cable. When longer cable connections are used, the attenuation of the travelling wave becomes larger and that causes frequency content in the signal at terminal far from the fault become lower. Due to this fact cut-off frequency used for systems with longer cable connections may be lower than the cut-off frequency used in this test network.

5.7 VSC HVDC scheme with overhead lines

Having investigated the fault location in cable based VSC HVDC systems, the feasibility of applying same measurement scheme for overhead line based systems in studied here. The capacitance of overhead lines is much lower than the capacitance of cables. Therefore, travelling waves are subjected to less attenuation when propagating along an overhead line. This generally makes the detection of faults in overhead lines easier compared to the cables. However, a simulation study was performed to confirm that travelling waves can be detected using the proposed Rogowski coil measurements of the surge capacitor currents, and determine the accuracy level.

For the simulation studies, the VSC HVDC system model used with the cable based system was modified by replacing the 300 km long cable with a 1000 km long overhead transmission line. The arrangement of the transmission line tower is shown in Figure 5-22. Frequency dependent

phase domain transmission line model available in PSCAD/EMTDC master library was used for simulating the transmission line [39]. Again, the simulations time step used for the simulations is 0.5μs.

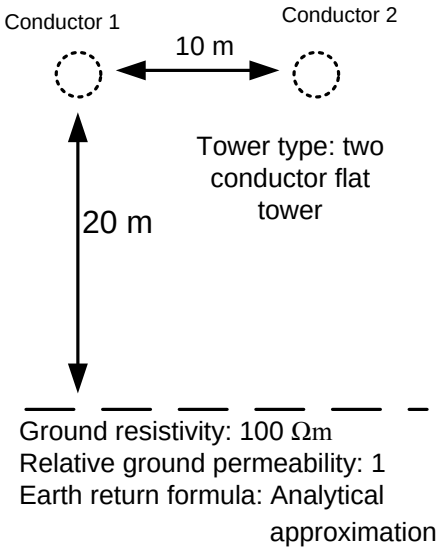

Figure 5-22Configurationof the transmission line

5.8 Fault location accuracies

Simulations were carried out using the same termination circuit proposed. Rogowski coil voltages of the two ends are used directly (without filtering) to determine the travelling wave arrival times of two ends. The accuracies were checked for different threshold settings. Figure 5-23 , Figure 5-24 and Figure 5-25 shows how the fault location accuracies vary with the threshold values, for three different solid faults at different distances from Converter-1. According to the results, any threshold with a margin with less than 30 times the pre-fault peak-to-peak signal would give excellent results for faults which are in the middle region (300 – 600 km) of the 1000 km overhead line. When the fault is close to one end, selecting very low

thresholds can increase the error. Thus for the system considered, a threshold with a margin between 10-30 times the pre-fault signal magnitude would be optimum under both low and high resistance faults.

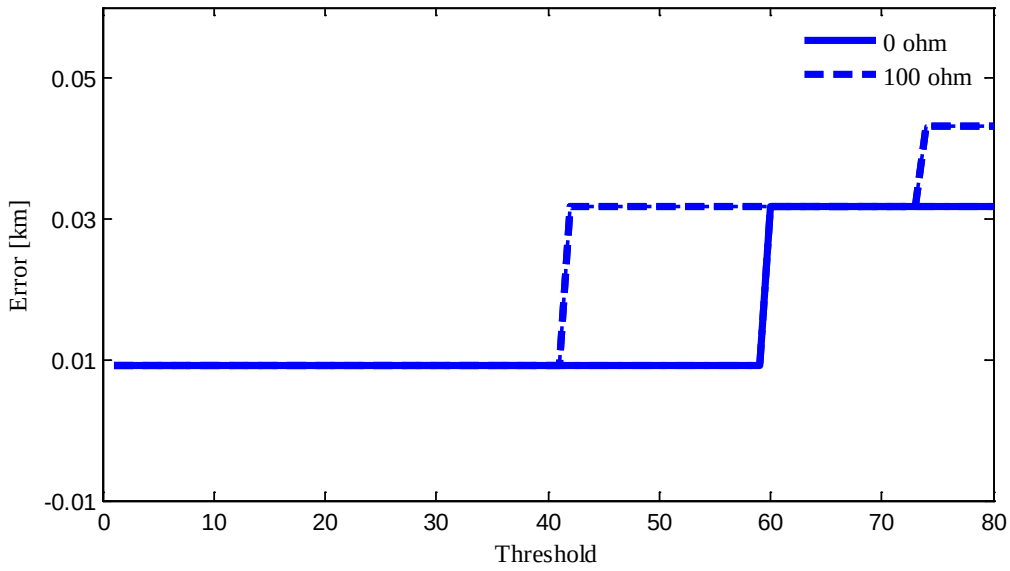

Figure 5-23 Variation of the fault location error with threshold for a fault 600 km away from the Converter-1.

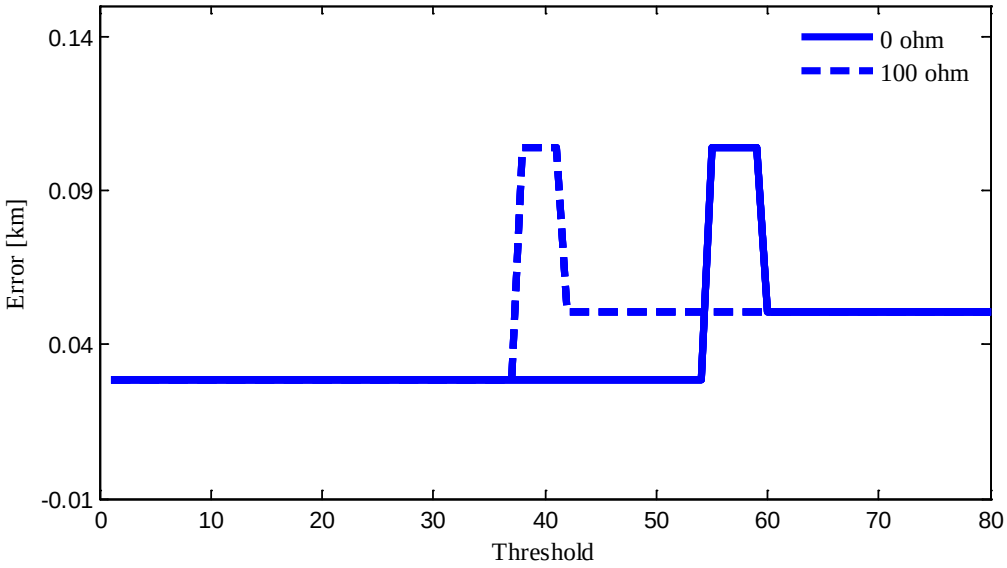

Figure 5-24 Variation of the fault location error with threshold for a fault 300 km away from the Converter-1.

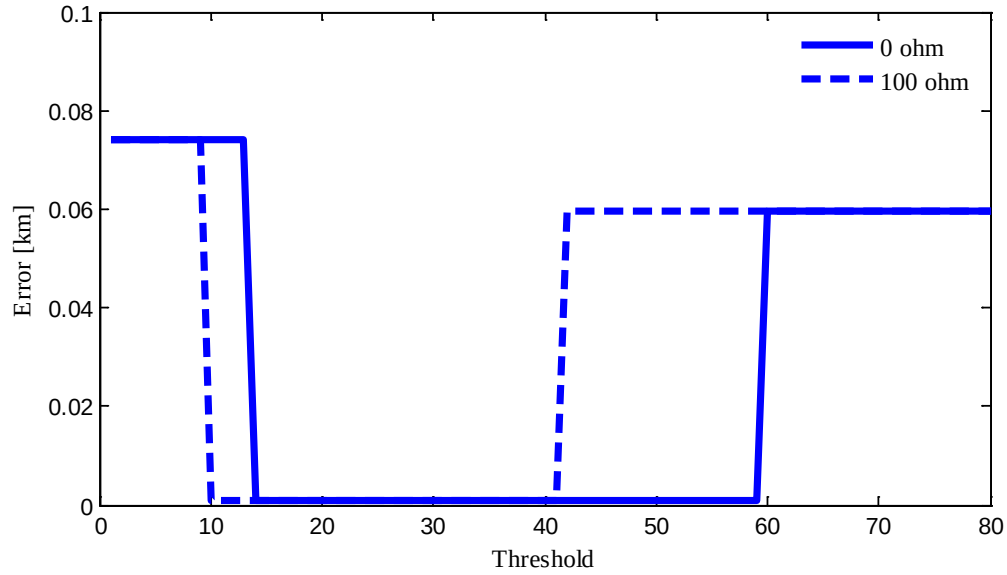

Figure 5-25 Variation of the fault location error with threshold for a fault 100 km away from the Converter-1

Simulation of many different faults along the line showed higher accuracy of fault location in the case of overhead line. Figure 5-26 and Figure 5-27 shows the fault location errors achieved with

Threshold-10 for pole-to-ground faults with 0 Ω and 100 Ω fault resistances respectively. Errors for the solid faults are less than 100 m. As for the long cable case, errors remain below 100 m when the fault resistance is increased.

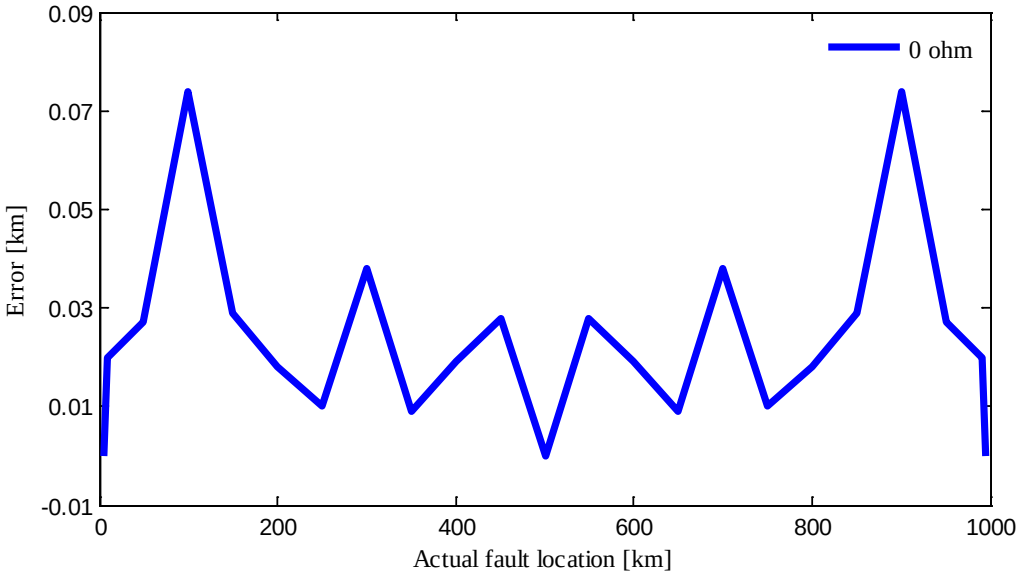

Figure 5-26 Fault location errors for solid faults along 1000 km overhead line.

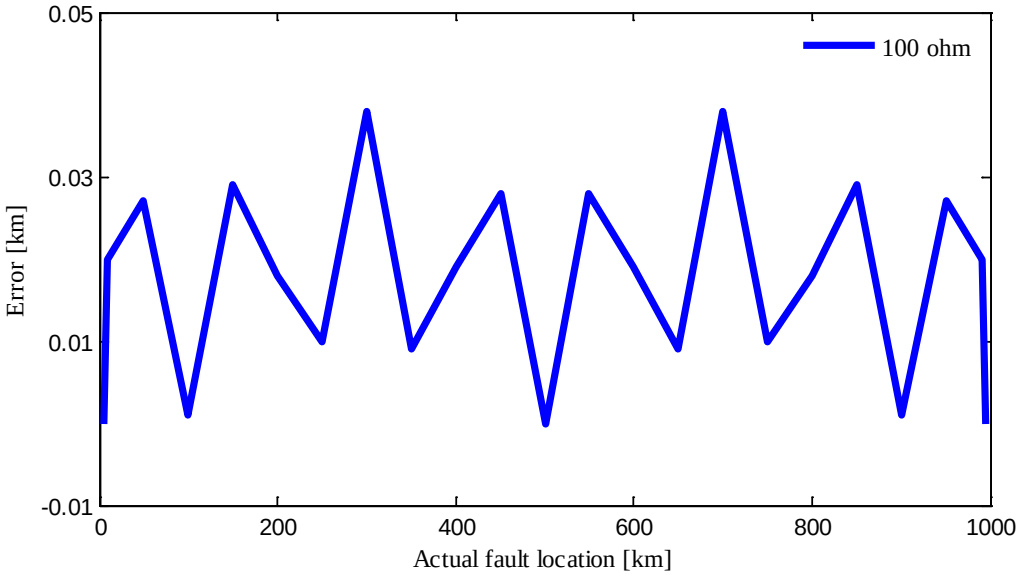

Figure 5-27 Fault location errors for faults with fault resistance of 100Ω along 1000 km overhead line

5.9 Concluding remarks

According to the simulation results, faults in a cable of a VSC HVDC scheme can be successfully located using double ended travelling wave based fault location method with the proposed travelling wave arrival detection scheme. The accuracy of the threshold based fault location depends on the threshold value used and the simulation results indicated that there is an optimum range that gives accurate results over a wide range of fault resistances. For the cable based HVDC system simulated in this study, selecting a threshold setting with a margin of 10 times the noise peak-to-peak magnitude gave the lowest errors for all the fault resistances considered.

Accuracy of fault location can be improved by filtering the signal from Rogowski coil with a low pass filter with a cut-off frequency of 50-100 kHz. With this approach, errors were less than 100 m for the VSC HVDC scheme with 300 km long cable. For overhead lines, as expected, a better accuracy could be achieved with the same measurement scheme even without filtering. Since the attenuation of the traveling waves in overhead transmission lines is much lower due to the low capacitance compared to cables, filtering the Rogowski coil signal to make the frequency ranges at both ends equal is not required. With the measurement scheme used fault locations could be calculated with errors less than 100 m for 1000 km overhead line. This is less than ±0.01% of error, and therefore has better accuracy than the accuracy reported in some previous work [41][42]. These accuracies were obtained only through simulation studies, however, experimental results presented in Chapter-3 indicates that the measurements schemes is feasible and has no particular challenges due to signal noise and interference.

The errors less than ±100 m are somewhat optimistic since the errors that should be considered in the practical implementation, such as D/A conversion errors and GPS clock errors were not represented in the simulations. Errors caused by these factors can be reduced with improved electronics. One can easily notice that although the theoretical error component due to sampling frequency cannot be eliminated, it can easily be reduced by selecting a higher sampling frequency, which will be limited only by the capability of the DAQ hardware. The accuracy obtained with the proposed method for both the test systems is better than the accuracy of existing line fault locators used in LCC HVDC schemes with lines/cables of similar lengths.

Chapter 6

Conclusions and Future Work

6.1 Conclusions

This thesis studied travelling wave based fault location for VSC HVDC schemes. The investigation was performed using a VSC HVDC system simulated in the EMT simulation software PSCAD/EMTDC.

Based on the assessment of different signals available for detection of the travelling wave arrival times, it can be concluded that:

- Both terminal voltage and surge capacitor current cannot be used for detection of travelling waves in a VSC HVDC scheme, if there are no series inductors at the transmission line or cable terminals. However, it is possible to use terminal currents as the detection signals, if they can be measured safely and economically.
- However, presence of a small series inductor as low 1 mH at the line/cable terminals enables successful detection of travelling waves using terminal voltage or surge capacitor current measurements.

- A Rogowski coil installed around the surge capacitor grounding circuit produces an ideal signal for detection of travelling waves. In addition to its ideal output signal, this method of measurement is also the safest, simplest and the most economical arrangement for practical implementation.
- Experimental measurements conducted at an existing LCC HVDC converter station confirmed that the Rogowski coil measurements of surge capacitor currents yield a signal with adequate magnitude and low noise level.

A Rogowski coil model suitable for EMT simulation was developed. Comparison of the output of this simulation model with actual measurements confirmed the accuracy of the simulation model for high frequency applications.

From the simulation studies carried out using a test network with a VSC HVDC system (and the associated measurement system) simulated in PSCAD/EMTDC software, the following conclusions can be made.

- Surge arrival time can be accurately determined by comparing the detection signal with a pre-set threshold.
- The accuracy of fault location is affected by the selected threshold value. For a given system, there is an optimum threshold level. At this optimum threshold level, the fault location accuracy is mostly independent of the fault resistance, and the distance to the fault.
- For a 400 kV, VSC HVDC system with a 300 km long cable, the optimum threshold value was about 10 times the peak-to-peak noise level observed during the steady state.
- Use of modal transformed signals to determine the fault location does not result in significant improvement in the accuracy for the VSC HVDC system studied in this thesis.

- The accuracy of fault location can be improved by low pass filtering the Rogowski coil voltage measurements before applying the thresholds. The optimum low pass filter cut-off frequency was in the range of 50-100 kHz for the cable based VSC HVDC system and the associated measurement system studied in this thesis.
- The same measurement arrangement can be used to detect and determine the travelling arrival times in overhead line based VSC HVDC systems. The same measurement system used on the 300 km cable system produced more accurate fault location results for a 1000 km long overhead line even without low pass filtering.
- Fault location accuracy of ±100 m can be achieved for a 1000 km overhead line or 300 km long cable in a VSC HVDC system with the proposed travelling wave arrival time measurement technique, with optimally selected thresholds and filtering.

6.2 Future work

Most practical VSC HVDC converters are based on the multi-level modular converter (MMC) technology. In MMC systems there are no large DC capacitors at the DC terminal of the converter, but the capacitance is distributed along the switching cells located inside the converter. Although no major problems are expected, the fault location method should be tested for this configuration as well.

As the VSC based multi-terminal HVDC grids are being considered for renewable energy harnessing. DC line faults on such DC grids would have severe consequences and therefore, fault location in such complex systems is highly important. Applicability of the proposed measurement technique for fault location in DC grids needs to be studied.

Bibliography

[1] M. M. Saha, J. Izykowski and E. Rosolowski. *Fault Location on Power Networks,* Springer, 2009.

[2] M. B. Dewe, S. Sankar and J. Arrillaga. "The application of satellite time references to HVDC fault location" *IEEE Transactions on Power Delivery*, vol. 8, no. 3, pp. 1295 – 1302, Jul. 1993.

[3] S. Guobing, C. Xinlei, G. ShuPing, S. Jiale and L. Guang. "Natural frequency based protection and fault location for VSC-HVDC transmission lines" *Proc. of the International Conference on Advanced Power System Automation and Protection,* Beijing, China, vol. 1, pp. 177 –182, 2011,.

[4] A. Elhaffar. "An optimized fault location system based on traveling waves for transmission networks" *Proc. of the16th IEEE Mediterranean Electrotechnical Conference (MELECON),* Yasmine Hammamet, Tunisia, pp. 954 –958, 2012,

[5] D. Novosel, D. G. Hart, E. Udren and J. Garitty, "Unsynchronized two-terminal fault location estimation," *IEEE Transactions on Power Delivery*, vol. 11, no. 1, pp. 130 –138, Jan. 1996.

[6] F. H. Magnago and A. Abur. "Fault location using wavelets" *IEEE Transactions on Power Delivery*, vol. 13, no. 4, pp. 1475 –1480, Oct. 1998.

[7] W. Zhao, Y. Song and W. Chen. "Improved GPS travelling wave fault locator for power cables by using wavelet analysis" *International Journal of Electrical Power & Energy Systems*, vol. 23, no. 5, pp. 403–411, Jun. 2001.

[8] Z. Q. Bo, G. Weller, F. Jiang and Q. X. Yang. "Application of GPS based fault location scheme for distribution system" *Proc. of the International Conference on Power System Technology*, Beijing, China, vol. 1, pp. 53 –57 vol.1,1998.

[9] P. Chen, B. Xu and J. Li. "A Traveling Wave Based Fault Locating System for HVDC Transmission Lines" *Proc. of the International Conference on Power System Technology*, Chongqing, China, pp. 1 –4, 2006.

[10] P. K. Murthy, J. Amarnath, S. Kamakshiah and B. P. Singh. “Wavelet Transform Approach for Detection and Location of Faults in HVDC System” *Proc. of the IEEE Region 10 and the Third international Conference on Information Systems*, Kharagpur, India, pp. 1 –6,2008,.

[11] J. Yang, J. E. Fletcher and J. O’Reilly. “Short-Circuit and Ground Fault Analyses and Location in VSC-Based DC Network Cables” *IEEE Transactions on Industrial Electronics*, vol. 59, no. 10, pp. 3827 –3837, Oct. 2012.

[12] J. Yang, J. E. Fletcher and J. O’Reilly. “Multi-terminal DC wind farm collection and transmission system internal fault analysis” *Proc. of the IEEE International Symposium on Industrial Electronics (ISIE)*, Bari, Italy, pp. 2437 –2442,2010,.

[13] Y.J. Kwon, S.H. Kang, D.G. Lee and H.K. Kim. “Fault Location Algorithm Based on Cross Correlation Method for HVDC Cable Lines” *Proc. of the IET 9th International Conference on Developments in Power System Protection*, Glasgow, UK, pp. 360 – 364,2008,.

[14] E. O. Schweitzer and M. Ando. “Single-ended transmission line fault locator” *U.S. Patent 476654923*, Aug-1988.

[15] M. M. Tawfik and M. M. Morcos. “ANN-based techniques for estimating fault location on transmission lines using Prony method” *IEEE Transactions on Power Delivery*, vol. 16, no. 2, pp. 219 –224, Apr. 2001.

[16] M. Joorabian, S. M. A. T.Asl and R. K. Aggarwal. “Accurate fault locator for EHV transmission lines based on radial basis function neural networks” *Electric Power Systems Research*, vol. 71, no. 3, pp. 195–202, Nov. 2004.

[17] K. Zimmerman and D. Costello. “Impedance-based fault location experience” *Proc. of the58th Annual Conference for Protective Relay Engineers*, Texas, USA, pp. 211 – 226, 2005.

[18] G. W. Swift. “The Spectra of Fault-Induced Transients” *IEEE Transactions on Power Apparatus and Systems*, vol. PAS-98, Issue. 3, pp. 940 –947, May 1979.

[19] Z. Chen, Z. Q. Bo, F. Jiang and G. Weller. “A fault generated high frequency current transients based protection scheme for series compensated lines” *Proc. of the Power Engineering Society Winter Meeting*, Singapore, vol. 3, pp. 1838 –1843, 2000.

[20] S. F. Huang and X. G. Wang. “A fault location scheme based on spectrum characteristic of fault-generated high-frequency transient signals” *Proc. of the Power Energy Society General Meeting,* Calgary, Canada, pp. 1 –5,2009,.

[21] K. P. Wang and K. Lee. “Visualizing wavelet transformed travelling waves on power transmission line using JAVA” *Proc. of the International Conference on Advances in Power System Control, Operation and Management,* vol. 2, pp. 349 – 353,*2000.*

[22] P. Chen, B. Xu and J. Li. “A Traveling Wave Based Fault Locating System for HVDC Transmission Lines” *Proc. of the International Conference on Power System Technology,* Chongqing, China, pp. 1 –4,2006,.

[23] X. Bing-yin, L. Jing and C. Ping. “Modern Traveling Wave Based Fault Location Technology and Its Application” *Trans. Tianjin Univ.*, vol. 14, no. 2, pp. 139–143, Apr. 2008.

[24] E. O. Schweitzer. “A Review of Impedance-Based Fault Locating Experience” *Proc. of the 15th Annual Western Protective Relay Conference,* Spokane, WA, October 1988.

[25] Y. Zhang, N. Tai and B. Xu. “Fault Analysis and Traveling-Wave Protection Scheme for Bipolar HVDC Lines” *IEEE Transactions on Power Delivery,* vol. 27, no. 3, pp. 1583 – 1591, Jul. 2012.

[26] M. A. Redfern, S. C. Terry and F. V. P. Robinson. “The application of distribution system current transformers for high frequency transient based protection” *Proc. of the8thIEE International Conference on Developments in Power System Protection,* Amsterdam, Netherland, vol. 1, pp. 108 – 111,2004.

[27] R. S. Popovic. “Hall devices for magnetic sensor microsystems” *Proc. of the International Conference on Solid State Sensors and Actuators,* Chicago, USA, vol. 1, pp. 377 –380, 1997,.

[28] J. Trontelj. “Optimization of integrated magnetic sensor by mixed signal processing” *Proc. of the16th IEEE Instrumentation and Measurement Technology Conference,* Venice, Italy, vol. 1, pp. 299–302, 1999,.

[29] J. D. Ramboz. “Machinable Rogowski coil, design, and calibration,” *IEEE Transactions on Instrumentation and Measurement,* vol. 45, no. 2, pp. 511 –515, Apr. 1996.

[30] P. F. Gale, P. V. Taylor, P. Naidoo, C. Hitchin and D. Clowes. “Travelling wave fault locator experience on Eskom’s transmission network” *Proc. of the* 7th*International Conference on Developments in Power System Protection*, Amsterdam, Netherland, pp. 327–330,2001.

[31] E. P. Suomalainen and J. K. Hallstrom. “Onsite Calibration of a Current Transformer Using a Rogowski Coil,” *IEEE Transactions on Instrumentation and Measurement*, vol. 58, no. 4, pp. 1054 –1058, Apr. 2009.

[32] L. Weibo, H. Hong, R. Jin, Z. Mingyuan and M. Minzhong. “A CT Centered on Rogowski Coil Applied for Low-Frequency Heavy Current Measurement” *Proc. of the International Conference on Electrical and Control Engineering (ICECE)* Wuhan, China, pp. 27 –30, 2010.

[33] L. A. Kojovic. “Split-core PCB Rogowski coil designs and applications for protective relaying” *Proc. of the Transmission and Distribution Conference and Exposition*, Dallas, USA, vol. 1, pp. 269 – 273 vol.1,2003,.

[34] D. A. Ward and J. L. T. Exon. “Using Rogowski coils for transient current measurements,” *Engineering Science and Education Journal*, vol. 2, no. 3, pp. 105 –113, Jun. 1993.

[35] C. Wang, Y. Chen, G. Zhang and Z. Zhou. “Design of Printed-Circuit Board Rogowski Coil for Highly Accurate Current Measurement” *Proc. of the International Conference on Mechatronics and Automation*, Harbin, China, pp. 3801 –3806,2007.

[36] G. Robles, M. Argueso, J. Sanz, R. Giannetti and B. Tellini. “Identification of parameters in a Rogowski coil used for the measurement of partial discharges” *IEEE Instrumentation and Measurement Technology Conference*, pp. 1 –4, *2007*, Warsaw, Poland.

[37] V. Dubickas and H. Edin. “High-Frequency Model of the Rogowski Coil With a Small Number of Turns,” *IEEE Transactions on Instrumentation and Measurement*, vol. 56, no. 6, pp. 2284 –2288, Dec. 2007.

[38] J. Zhu, L. Yang, J. Jia and Q. Zhang. “The design of Rogowski coil with wide band using for partial discharge measurements” *Proc. of the International Symposium on*

Electrical Insulating Materials (ISEIM 2005), Kitakyushu, Japan, vol. 2, pp. 518 – 521, 2005.

[39] F. Castellanos and J. R. Marti. “Full frequency-dependent phase-domain transmission line model,” *IEEE Transactions on Power Systems*, vol. 12, no. 3, pp. 1331 –1339, Aug. 1997.

[40] Z. Yi-ning, L. Y. Hao, X. Min and C. Z. Xiang. “A novel algorithm for HVDC line fault location based on variant travelling wave speed” *Proc. of the4th International Conference on Electric Utility Deregulation and Restructuring and Power Technologies (DRPT)*, Weihai, China, pp. 1459 –1463,2011,.

[41] Y.J. Kwon, S.H. Kang, D.G. Lee and H.K. Kim. “Fault Location Algorithm Based on Cross Correlation Method for HVDC Cable Lines” *Proc. of the9th International Conference on Developments in Power System Protection*, Glasgow, UK, pp. 360 – 364,2008.

[42] S. G. Bing, C. X. Lei, G. S. Ping, S. J. Le and L. Guang. “Natural frequency based protection and fault location for VSC-HVDC transmission lines” *Proc. of the International Conference on Advanced Power System Automation and Protection (APAP)*, Beijing, China, vol. 1, pp. 177 –182,2011.